JGR Space Physics

RESEARCH ARTICLE
10.1029/2019JA027007

Key Points:
- Heavy ion precipitation into the Jovian atmosphere can produce the observed auroral X-ray emission
- Using Juno measurements of ion fluxes over Jupiter's pole, we simulate X-ray spectra
- We compare our approximated synthetic X-ray spectra produced by in situ data to observed emission

Supporting Information:
- Supporting Information S1
- Supporting Information S2

Correspondence to:
T. E. Cravens,
cravens@ku.edu

Citation:
Houston, S. J., Cravens, T. E., Schultz, D. R., Gharibnejad, H., Dunn, W. R., Haggerty, D. K., et al. (2020). Jovian auroral ion precipitation: X-ray production from oxygen and sulfur precipitation. *Journal of Geophysical Research: Space Physics*, *125*, e2019JA027007. https://doi.org/10.1029/2019JA027007

Received 11 JUN 2019
Accepted 13 OCT 2019
Accepted article online 9 DEC 2019

Jovian Auroral Ion Precipitation: X-Ray Production From Oxygen and Sulfur Precipitation

S. J. Houston[1,2], T. E. Cravens[1], D. R. Schultz[3,4], H. Gharibnejad[3,5], W. R. Dunn[6,7,8], D. K. Haggerty[9], A. M. Rymer[9], B. H. Mauk[9], and N. Ozak[1,10]

[1]Department of Physics and Astronomy, University of Kansas, Lawrence, KS, USA, [2]Now at The Johns Hopkins University Applied Physics Laboratory, Laurel, MD, USA, [3]Department of Physics, University of North Texas, Denton, TX, USA, [4]Now at Department of Physics and Astronomy, Northern Arizona University, Flagstaff, AZ, USA, [5]Now at National Institute of Standards and Technology, Gaithersburg, MD, USA, [6]Mullard Space Science Laboratory, University College London, London, UK, [7]Center for Planetary Science, University College London, London, UK, [8]Harvard-Smithsonian Center for Astrophysics, Cambridge, MA, USA, [9]The Johns Hopkins University Applied Physics Laboratory, Laurel, MD, USA, [10]CluePoint S.A., Axis Parc, Mont-Saint-Guibert, Belgium

Abstract Many attempts have been made to model X-ray emission from both bremsstrahlung and ion precipitation into Jupiter's polar caps. Electron bremsstrahlung modeling has fallen short of producing the total overall power output observed by Earth-orbit-based X-ray observatories. Heavy ion precipitation was able to reproduce strong X-ray fluxes, but the proposed incident ion energies were very high (>1 MeV per nucleon). Now with the Juno spacecraft at Jupiter, there have been many measurements of heavy ion populations above the polar cap with energies up to 300–400 keV per nucleon (keV/u), well below the ion energies required by earlier models. Recent work has provided a new outlook on how ion-neutral collisions in the Jovian atmosphere are occurring, providing us with an entirely new set of impact cross sections. The model presented here simulates oxygen and sulfur precipitation, taking into account the new cross sections, every collision process, the measured ion fluxes above Jupiter's polar aurora, and synthetic X-ray spectra. We predict X-ray fluxes, efficiencies, and spectra for various initial ion energies considering opacity effects from two different atmospheres. We demonstrate that an in situ measured heavy ion flux above Jupiter's polar cap is capable of producing over 1 GW of X-ray emission when some assumptions are made. Comparison of our approximated synthetic X-ray spectrum produced from in situ particle data with a simultaneous X-ray spectrum observed by XMM-Newton shows good agreement for the oxygen part of the spectrum but not for the sulfur part.

1. Introduction

The National Aeronautics and Space Administration's Juno mission has, at the time of this writing, been orbiting Jupiter for nearly 3 years. Since arrival, Juno has arguably uncovered more questions than it has answered, although its discoveries have been numerous. In its time spent at Jupiter, Juno has put greater constraints on the gravitational field (Folkner et al., 2017; Iess et al., 2018), measured a magnetic field with substantial complexity (Connerney et al., 2017, 2018; Moore et al., 2018), and returned images of Jupiter detailing the intricate features seen in the cloud tops (Orton et al., 2017; Sánchez-Lavega et al., 2018). Most importantly to this paper, Juno has been able to measure heavy ions above the polar caps that indicate they are precipitating into the top of the atmosphere (Clark, Mauk, Haggerty, et al., 2017; Clark, Mauk, Paranicas, et al., 2017; Haggerty et al., 2017), potentially producing Jupiter's dynamic X-ray aurorae.

X-ray production at Jupiter has been of interest to the space physics community from when it was first observed by the Einstein Observatory in April of 1979 (Metzger et al., 1983). Although Metzger et al. (1983) were unable to distinguish a line spectrum from a continuum due to the limitations of the detector, they proposed that the primary source of X-rays must be coming from heavy ion precipitation, stating, “the shape of the response and the observed X-ray power indicate that the source of this auroral emission is not electron bremsstrahlung as on the earth, but is most probably line emission from O and S ions with energies between 0.03 and 4.0 MeV/nucleon ....” Now, with the Juno spacecraft orbiting Jupiter, oxygen and sulfur ions have been measured above the polar caps with energies up to 400 keV per nucleon (keV/u) (Clark, Mauk, Haggerty, et al., 2017; Clark, Mauk, Paranicas, et al., 2017; Haggerty et al., 2017).

In the past, attempts were made to reproduce the X-ray emission observed at Jupiter with ion precipitation models (Cravens et al., 1995, 2003; Ozak et al., 2010, 2013), but they required very high energy ions (>1.2 MeV/u) to sufficiently strip the ions of their electrons in order to produce the observed X-ray emissions. But this could be overlooked because no in situ measurements of the ion energies above the polar cap existed. However, such ion measurements are now available thanks to Juno; and a more complete treatment of the underlying atomic collision processes now exists (Schultz et al., 2019). Incorporated into our ion-precipitation models, these new cross sections demonstrate the "threshold" ion energy necessary to produce X-ray yielding excited states is significantly less (on the order of 200 keV/u) than the earlier cross sections gave. This difference arises largely from the improved treatment of ion energy loss in the new atomic data, evidenced by an increased stopping power derived from ion-transport simulations for ion energies between 50 and 2,000 keV/u that is now in better agreement with recommended values. The more complete treatment also results in a shift in the equilibrium distribution of charge states toward lower energies and motivated consideration of X-ray production from direct ion excitation in addition to that from charge transfer.

We expand on the ion precipitation models that have come before (Cravens et al., 1995; Houston et al., 2018; Ozak et al., 2010, 2013), modeling oxygen from 10 keV/u to 25 MeV/u and sulfur between 10 keV/u and 2 MeV/u, in an attempt to explain the X-ray emission from the Jovian polar caps. We consider all charge states of oxygen, including the negative charge state (O^{q+}, $q = -1, 0, \dots, 8$) and all sulfur positive charge states (S^{q+}, $q = 0, \dots, 16$). Ultimately, O^{6+}, O^{7+}, and S^{6+}-S^{15+} are the most important charge states to consider when producing X-rays, because their ionization potentials are great enough to emit X-ray photons.

We first discuss the differences between our model and the models by Houston et al. (2018), Ozak et al. (2010), and Ozak et al. (2013). We then introduce new ion-neutral collision processes that account for the vast contrast in our results and those presented by our predecessors. Various techniques used within the model are explained, and ion flux measurements made by the Jupiter Energetic Particle Detector Instrument (JEDI) (Mauk et al., 2017) are displayed. Results are given for a variety of monoenergetic ion beam energies, including several ion production rates, X-ray efficiencies, and example X-ray spectra with opacity effects. The JEDI measurements are input into the model, and results indicating X-ray production are shown. We compare our modeled spectrum with a simultaneous XMM-Newton spectrum observed during the same window within which the ion precipitation was detected by Juno. Finally, we conclude with a discussion on the implications of the model results.

The observed X-ray aurora has shown a strange complexity. For example, in ~30% of observations, the X-ray aurora pulses with a regular period on the order of tens of minutes as reported by Dunn et al. (2016; 2017), Gladstone et al. (2002), and Jackman et al. (2018); however, during other observations, the emission is either continuous or the pulses are erratic, with no clear periodic signature (Branduardi-Raymont et al., 2007; Elsner et al., 2005). Therefore, when analyzing heavy ion measurements made by JEDI, it is important to consider that this emission is highly temporally and spatially variable and that the associated ion precipitation may also vary with time. One must remember that every energy spectrum and flux intensity of oxygen and sulfur is unique. Sometimes, oxygen fluxes are measured with a higher intensity, while at other times, sulfur fluxes are higher. Each collection of data greatly depends on the time and location of where it is made. Given that each flight of Juno over the polar regions follows a different flight path, it is also difficult to differentiate spatial and temporal changes in the measurements. Thus, when using the JEDI flux measurements, they need to be fine-tuned for every case.

2. Physical Processes and Model Description

The basic simulation methods used for this paper have been described in great detail by Houston et al. (2018) and Ozak et al. (2010, 2013), and the references therein. When Ozak et al. (2010) first published results, they showed X-ray production rates from precipitating oxygen and sulfur, and then Ozak et al. (2013) made predictions of field-aligned currents and airglow intensities that Juno would measure when it arrived to Jupiter, and Houston et al. (2018) primarily focused on field-aligned current and ultraviolet emission from oxygen. We follow up on the promise made in Houston et al. (2018) to include energetic sulfur precipitation and oxygen improvements, with proton precipitation being left to a future and very necessary publication.

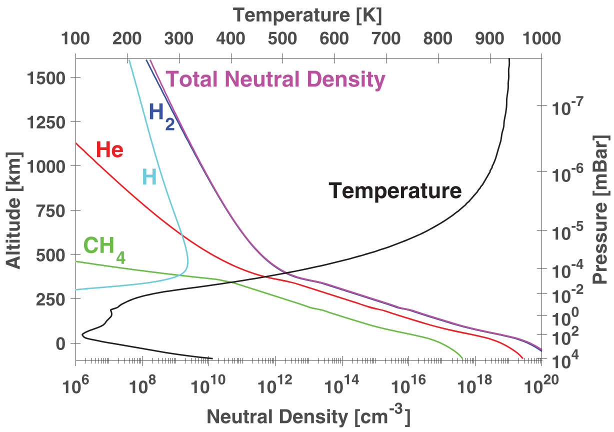

Figure 1. Atmospheric density profiles of H_2, He, CH_4, and H based on data shown in Maurellis and Cravens (2001) and Sinclair et al. (2018). Also shown is the neutral temperature profile as a function of altitude and pressure.

Aside from optimization improvements, the main contrast between the current model and earlier versions can be summarized as follows:

- The Jovian atmosphere has been extended deeper, down below the 1 bar level.
- Atomic data (principally inelastic collision cross sections) for oxygen ions colliding with H_2 previously (Ozak et al., 2013; Schultz et al., 2017) only considered processes that occurred involving electronic transitions of projectile electrons or target electrons nonsimultaneously (denoted "NSIM" processes). A more complete treatment for oxygen (Schultz et al., 2019) ion impact expands the model to include simultaneous (SIM) processes that occur involving both target and projectile electron transitions.
- Analogous atomic data for sulfur ion impact of H_2 have also been created (still preliminary and not yet published) that include treatment of SIM processes, updating the purely NSIM processes considered in Ozak et al. (2013), and have been incorporated in the present work from the preliminary analysis of the data to be published.
- X-ray efficiencies and approximations to synthetic X-ray spectra that include opacity effects are presented with both the current atmosphere and an upper limit, fully mixed atmosphere.
- The direct excitation mechanism now also contributes to X-ray production, increasing the number of X-rays produced.
- Juno data (both oxygen and sulfur flux measurements) are adapted and input into the simulation.

2.1. Jovian Atmosphere

Houston et al. (2018) used a neutral atmosphere originally presented by Maurellis and Cravens (2001) based on Galileo probe data (Seiff et al., 1996, 1997) and remote observations (Sada et al., 1998). The same atmosphere is used here, only we have extended the depth from 200 to −88 km, where 0 km is set to where the pressure is equal to 1 bar (Figure 1). The atmosphere below 200 km has been generated using temperature-pressure profiles retrieved from National Aeronautics and Space Administration's Infrared Telescope Facility and the Texas Echelon Cross Echelle Spectrograph Instrument (Sinclair et al., 2018). Using the temperature and pressure, the ideal gas law is then solved to obtain the total number density. Because we are below the homopause, where a well-mixed atmosphere is present, the mixing ratios from 200 km are extended down to −88 km to calculate the number density of each species.

There has been much speculation about the composition of the upper atmosphere over the polar caps (see section 5.2 of Clark et al., 2018; Gérard et al., 2014; and Parkinson et al., 2006). To help account for this, we generate a second atmospheric profile (not displayed) by taking the mixing ratio of molecular hydrogen to helium and methane at the bottom of the density profile in Figure 1 and then redistribute the helium and methane from the top of the atmosphere with that same mixing ratio. This allows for a completely well-mixed atmosphere that ignores a defined homopause; rather, the entire atmosphere is homogeneous. The H_2 distribution of this atmosphere remains the same as that in Figure 1; thus, ion precipitation will not be affected because only ion collisions in a hydrogen gas are considered. However, when photoemission is discussed, the well-mixed atmosphere will have greater photoabsorption effects. Atomic hydrogen is ignored in the well-mixed atmosphere because of how chemically active it tends to be (as can be seen in the original atmosphere, below the homopause), and it is not unreasonable to think the column density of H will have negligible effects on the opacity of X-ray emission, as it does in the original atmosphere. We will refer to the atmosphere displayed in Figure 1 as Atmosphere 1 and the well-mixed atmosphere as Atmosphere 2.

2.2. Ion-Neutral Impact Processes

Houston et al. (2018) modeled oxygen precipitation using the nine relevant NSIM processes as the ion traversed the upper atmosphere using the atomic data describing the rates of these processes and the energy loss for each process as a function of ion energy given by Schultz et al. (2017), summarized here:

$$O^{q+} + H_2 \rightarrow \begin{cases} O^{q+} + H_2^{+} + e & \text{Single Ionization} \\ O^{q+} + 2H^{+} + 2e & \text{Double Ionization} \end{cases} \tag{1a}$$

$$O^{q+} + H_2 \rightarrow \begin{cases} O^{(q-1)+} + \begin{cases} H_2^+ & \text{Single Capture} \\ H^+ + H^+ + e & \text{Transfer Ionization} \end{cases} \\ O^{(q-2)+} + \begin{cases} 2H^+ \rightarrow O^{(q-1)+} + e & \text{Double Capture} - \text{Autoionization} \\ H^+ + H^+ & \text{Double Capture} \end{cases} \end{cases} \tag{1b}$$

$$O^{q+} + H_2 \rightarrow \begin{cases} O^{(q+1)} + H_2^+ + 2e; H + H^+ + 2e & \text{Single Stripping} \\ O^{(q+2)} + H_2^+ + 3e; H + H^+ + 3e & \text{Double Stripping} \end{cases} \tag{1c}$$

$$O^{q+} + H_2 \rightarrow O^{q+} + H_2^*; H^* + H^* \quad \text{Electronic Excitation - All States} \tag{1d}$$

However, as noted above, treatment of processes that involve electron transitions on both target and projectile simultaneously has subsequently lead to fundamental improvements of the oxygen and sulfur data (Schultz et al., 2019). The NSIM and SIM processes represented by this expanded consideration, utilized in the present ion precipitation model, are the following:

$$\begin{aligned}
&\mathrm{X}^{q+} + \mathrm{H}_2 \rightarrow \mathrm{X}^{q+} + \mathrm{H}_2^+ + \mathrm{e}; \mathrm{X}^{q+} + \mathrm{H} + \mathrm{H}^+ + \mathrm{e} && \text{single ionization (SI)} \\
&\mathrm{X}^{q+} + \mathrm{H}_2 \rightarrow \mathrm{X}^{q+*} + \mathrm{H}_2^+ + \mathrm{e}; \mathrm{X}^{q+*} + \mathrm{H} + \mathrm{H}^+ + \mathrm{e} && \text{SI + single projectile excitation (SI+SPEX)} \\
&\mathrm{X}^{q+} + \mathrm{H}_2 \rightarrow \mathrm{X}^{q+**} + \mathrm{H}_2^+ + \mathrm{e}; \mathrm{X}^{q+**} + \mathrm{H} + \mathrm{H}^+ + \mathrm{e} && \text{SI + double projectile excitation (SI+DPEX)} \\
&\mathrm{X}^{q+} + \mathrm{H}_2 \rightarrow \mathrm{X}^{(q+1)+} + \mathrm{H}_2^+ + 2\mathrm{e}; \mathrm{X}^{(q+1)+} + \mathrm{H} + \mathrm{H}^+ + 2\mathrm{e} && \text{SI + single stripping (SI+SS)} \\
&\mathrm{X}^{q+} + \mathrm{H}_2 \rightarrow X^{(q+2)+} + \mathrm{H}_2^+ + 3\mathrm{e}; \mathrm{X}^{(q+2)+} + \mathrm{H} + \mathrm{H}^+ + 3\mathrm{e} && \text{SI + double stripping (SI+DS)}
\end{aligned}$$

$$\begin{aligned}
&\mathrm{X}^{q+} + \mathrm{H}_2 \rightarrow \mathrm{X}^{q+} + \mathrm{H}^+ + \mathrm{H}^+ + 2\mathrm{e} && \text{double ionization (DI)} \\
&\mathrm{X}^{q+} + \mathrm{H}_2 \rightarrow \mathrm{X}^{q+*} + \mathrm{H}^+ + \mathrm{H}^+ + 2\mathrm{e} && \text{DI+SPEX} \\
&\mathrm{X}^{q+} + \mathrm{H}_2 \rightarrow \mathrm{X}^{q+**} + \mathrm{H}^+ + \mathrm{H}^+ + 2\mathrm{e} && \text{DI+DPEX} \\
&\mathrm{X}^{q+} + \mathrm{H}_2 \rightarrow \mathrm{X}^{(q+1)+} + \mathrm{H}^+ + \mathrm{H}^+ + 3\mathrm{e} && \text{DI+SS} \\
&\mathrm{X}^{q+} + \mathrm{H}_2 \rightarrow \mathrm{X}^{(q+2)+} + \mathrm{H}^+ + \mathrm{H}^+ + 4e && \text{DI+DS}
\end{aligned}$$

$$\begin{aligned}
&\mathrm{X}^{q+} + \mathrm{H}_2 \rightarrow \mathrm{X}^{(q-1)+} + \mathrm{H}^+ + \mathrm{H}^+ + \mathrm{e} && \text{transfer ionization (TI)} \\
&\mathrm{X}^{q+} + \mathrm{H}_2 \rightarrow \mathrm{X}^{(q-1)+*} + \mathrm{H}^+ + \mathrm{H}^+ + \mathrm{e} && \text{TI+SPEX} \\
&\mathrm{X}^{q+} + \mathrm{H}_2 \rightarrow \mathrm{X}^{(q-1)+**} + \mathrm{H}^+ + \mathrm{H}^+ + \mathrm{e} && \text{TI+DPEX} \\
&\mathrm{X}^{q+} + \mathrm{H}_2 \rightarrow \mathrm{X}^{q+} + \mathrm{H}^+ + \mathrm{H}^+ + 2\mathrm{e} && \text{TI+SS} \\
&\mathrm{X}^{q+} + \mathrm{H}_2 \rightarrow \mathrm{X}^{(q+1)+} + \mathrm{H}^+ + \mathrm{H}^+ + 3\mathrm{e} && \text{TI+DS}
\end{aligned}$$

$$\begin{aligned}
&\mathrm{X}^{q+} + \mathrm{H}_2 \rightarrow \mathrm{X}^{(q-2)+**} + \mathrm{H}^+ + \mathrm{H}^+ \rightarrow \mathrm{X}^{(q-1)+} + \mathrm{e} && \text{double capture autionization (DCAI)} \\
&\mathrm{X}^{q+} + \mathrm{H}_2 \rightarrow \mathrm{X}^{(q-2)+***} + \mathrm{H}^+ + \mathrm{H}^+ \rightarrow \mathrm{X}^{(q-1)+*} + \mathrm{e} && \text{DCAI+SPEX} \\
&\mathrm{X}^{q+} + \mathrm{H}_2 \rightarrow \mathrm{X}^{(q-2)+****} + \mathrm{H}^+ + \mathrm{H}^+ \rightarrow \mathrm{X}^{(q-1)+**} + \mathrm{e} && \text{DCAI+DPEX} \\
&\mathrm{X}^{q+} + \mathrm{H}_2 \rightarrow \mathrm{X}^{(q-2)+**} + \mathrm{H}^+ + \mathrm{H}^+ \rightarrow \mathrm{X}^{q+} + 2\mathrm{e} && \text{DCAI+SS} \\
&\mathrm{X}^{q+} + \mathrm{H}_2 \rightarrow \mathrm{X}^{(q-2)+**} + \mathrm{H}^+ + \mathrm{H}^+ \rightarrow \mathrm{X}^{(q+1)+} + 3\mathrm{e} && \text{DCAI+DS}
\end{aligned}$$

$$\begin{aligned}
&\mathrm{X}^{q+} + \mathrm{H}_2 \rightarrow \mathrm{X}^{(q-1)+} + \mathrm{H}_2^+; \mathrm{X}^{(q-1)+} + \mathrm{H} + \mathrm{H}^+ && \text{single electron capture (SC)} \\
&\mathrm{X}^{q+} + \mathrm{H}_2 \rightarrow \mathrm{X}^{(q-1)+*} + \mathrm{H}_2^+; \mathrm{X}^{(q-1)+*} + \mathrm{H} + \mathrm{H}^+ && \text{SC+SPEX} \\
&\mathrm{X}^{q+} + \mathrm{H}_2 \rightarrow \mathrm{X}^{(q-1)+**} + \mathrm{H}_2^+; \mathrm{X}^{(q-1)+**} + \mathrm{H} + \mathrm{H}^+ && \text{SC+DPEX} \\
&\mathrm{X}^{q+} + \mathrm{H}_2 \rightarrow \mathrm{X}^{q+} + \mathrm{H}_2^+ + \mathrm{e}; \mathrm{X}^{q+} + \mathrm{H} + \mathrm{H}^+ + \mathrm{e} && \text{SC+SS} \\
&\mathrm{X}^{q+} + \mathrm{H}_2 \rightarrow \mathrm{X}^{(q+1)+} + \mathrm{H}_2^+ + 2\mathrm{e}; \mathrm{X}^{(q+1)+} + \mathrm{H} + \mathrm{H}^+ + 2\mathrm{e} && \text{SC+DS}
\end{aligned}$$

$X^{q+} + H_2 \rightarrow X^{(q-2)+} + H^+ + H^+$	double electron capture (DC)
$X^{q+} + H_2 \rightarrow X^{(q-2)+*} + H^+ + H^+$	DC+SPEX
$X^{q+} + H_2 \rightarrow X^{(q-2)+**} + H^+ + H^+$	DC+DPEX
$X^{q+} + H_2 \rightarrow X^{(q-1)+} + H^+ + H^+ + e$	DC+SS
$X^{q+} + H_2 \rightarrow X^{q+} + H^+ + H^+ + 2e$	DC+DS
$X^{q+} + H_2 \rightarrow X^{q+} + H_2^*$	target excitation (TEX)
$X^{q+} + H_2 \rightarrow X^{q+*} + H_2^*$	TEX+SPEX
$X^{q+} + H_2 \rightarrow X^{q+**} + H_2^*$	TEX+DPEX
$X^{q+} + H_2 \rightarrow X^{(q+1)+} + H_2^* + e$	TEX+SS
$X^{q+} + H_2 \rightarrow X^{(q+2)+} + H_2^* + 2e$	TEX+DS

where X stands for the projectile, either O or S. q is the charge state and depends on the number of electrons bound to the ion; q runs from 0 to 8 for O and from 0 to 16 for S. The abbreviations for each process shown here are used throughout the rest of the paper. Some processes are not possible for neutral or singly ionized atoms or, similarly, for fully stripped or O^{7+} and S^{15+} ions (e.g., for neutral O and S capture of two electrons, DC, cannot occur and for the fully stripped ions O^{8+} and S^{16+}, neither single or double stripping, SS or DS, is possible). We also include the negative ion channel, that is, production and destruction of O^-, as described by Schultz et al. (2019), owing to the importance to the charge state distribution at low energy, and implications for its presence in atmospheric chemical models. We use a single, NSIM process that can bring O to O^-, governed by the cross sections in Table C of Schultz et al. (2019). Once in the negative charge state, six processes are considered: SI, SI+SS, DI, DI+SS, TEX, and TEX+SS. For more details, see Section 3.4 given by Schultz et al. (2019). Furthermore, S^- was not calculated because the importance of that channel to the ion fraction populations of S, S^+, and possibly S^{2+} were not realized at the time of the calculations but subsequently identified for O^- production (Schultz et al., 2019) for which explicit measurements exist for the ion fraction distributions of O^-, O, O^+, and O^{2+} to test inclusion of the O^- production and destruction channels. For the present work, inclusion of the corresponding channels for S^- would be relevant for only the lowest energy portion of the ion energy range considered, not significantly affecting the energy loss and ion fraction population except at the lowest portion of this energy range and not significantly influencing the X-ray production (little comes from excitation of S or S^+ at these low impact energies).

Details of the atomic collision model and calculations have been given by Schultz et al. (2019) as well as explanation of the improvements to ion and electron transport models due to inclusion of SIM processes. As noted above, important for the present work is the fact that the more complete atomic collision model has shifted the peaks of the ion charge state distribution to lower ion energies and has motivated consideration of the additional X-ray production mechanism and direct projectile excitation, in addition to the previously considered X-ray emission subsequent to charge transfer.

2.3. Charge State Equilibrium Fractions

In a very broad sense, as an ion precipitates through the atmosphere, each collision with an atmospheric gas molecule or atom can result in four different outcomes for the projectile. The ion can become excited through NSIM or SIM processes (e.g., SPEX or SPEX+SI), become further ionized (e.g., NSIM or SIM SS or DS), gain an electron or two (e.g., NSIM or SIM SC or TI), or can maintain its charge while affecting the target (e.g., NSIM SI or TEX). Each type of interaction is governed by the energy of the precipitating ion; that is, a more energetic ion will generally be stripped of more electrons than one precipitating with less energy. By knowledge of the stripping and charge transfer cross sections, it is possible to calculate the equilibrium fractions of each charge state versus the ion energy. This is done using transition probabilities, P_{ij}:

$$\phi^i_q(E)P^i_{q,q+1} = \phi^i_{q+1}(E)P^i_{q+1,q}, \tag{2}$$

where $\phi^i_q(E)$ is the fraction of ions in charge state q, at energy E, for species i, either oxygen or sulfur. $P^i_{q,q+1}$ denotes the sum of the stripping cross sections and $P^i_{q+1,q}$, the sum of the charge transfer cross sections, for species i. A normalization is given by the condition of each energy

$$\sum_{q=q_0}^{q=Z}\phi^i_q(E) = 1, \tag{3}$$

where q_0 denotes the lowest charge state for species i, $q_0 = -1$ for O and $q_0 = 0$ for S, $Z = 8$ and 16 are the nuclear charges for O and S, and $\phi_q^i(E)$ is the charge state fraction. These are shown for oxygen and sulfur as a function of energy in Figures 2 and 3.

The charge state equilibrium fractions demonstrate at what energy the ion will reach a given charge state regardless of the sequence of collision processes undergone or the initial ion energy; the ion history is immediately forgotten. From these fractions, one can quickly see what energies are required for an ion to begin producing X-rays. For both oxygen and sulfur, the sixth charge state must be reached to begin producing X-rays (O^{6+} and S^{6+} with projectile excitation or O^{7+} and S^{7+} via charge exchange). These charge states are sufficiently reached for both species at an energy between 200 and 300 keV/u, where they become the most probable charge state for the given energy (a total energy of ~3.2 and ~6.4 MeV for oxygen and sulfur, respectively). These newly developed equilibrium fractions supersede previous models presented by Ozak et al. (2010) and Houston et al. (2018), which showed an O^{6+} peak at nearly 1 MeV/u and an S^{6+} peak at 600 keV/u.

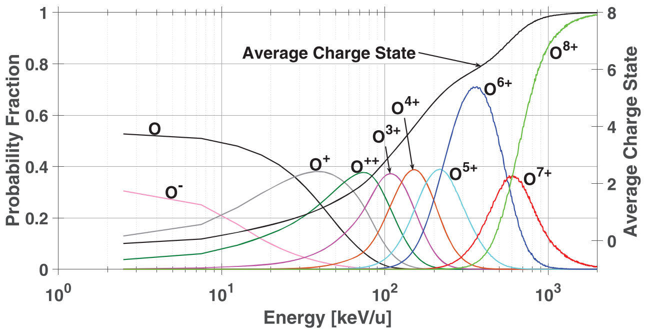

Figure 2. Oxygen charge state distribution as a function of ion energy. The high charge state peaks have dramatically shifted to lower energies than previous models produced. Houston et al. (2018) and Ozak et al. (2010) had the peak of O^{6+} at ~900 keV/u; however, due to the use of newly developed SIM cross sections, the peak has now shifted down to an energy of ~350 keV/u.

Relative to the previous results, it now requires less energy to produce charge states capable of emitting X-rays and the ions are not penetrating the atmosphere as deeply as was previously modeled because more energy is being lost in the middle energy range (between 50 and 2,000 keV/u; see the stopping power discussion given by Schultz et al., 2019), affecting the depth effects and predicted X-ray spectra.

2.4. Depth Effects

The opacity of the Jovian atmosphere is incorporated into the model using the optical depth of outgoing X-ray photons. We look at three different path angles, 0°, 80°, and 90° (where the angle is measured with respect to the axis of rotation), and with two atmospheric profiles; the density profile shown in Figure 1 and a well-mixed atmosphere as discussed in section 2.1. The optical depth is given by

$$\tau(\lambda, z_0) = Ch(\theta, z_0) \sum_j \sigma_j^{\text{abs}}(\lambda) \int_{z_0}^{\infty} n_j(z)\text{d}z, \tag{4}$$

where $\tau(\lambda, z_0)$ is the optical depth as a function of emitted photon wavelength, λ, and the altitude at which the emission occurred, z_0. $Ch(\theta, z_0)$ is the Chapman function, dependent upon the photon path angle, θ, and the altitude. $\sigma_j^{\text{abs}}(\lambda)$ is the absorption cross section summed over each species, j (H_2, He, and CH_4), and is a function of wavelength. For example, the absorption cross section at a photon energy of 100 eV is 3.7×10^{-20}, 2.8×10^{-19}, and 4.4×10^{-19}, for H_2, He, and CH_4, respectively, and continues to decrease in value through 10 keV (with the exception of a sharp spike in CH_4 at 283 eV, due to the K-shell edge) (Cravens et al., 2006). $n_j(z)$ is the neutral density of each atmospheric constituent as a function of altitude, integrated from the point of emission out through the top of the atmosphere.

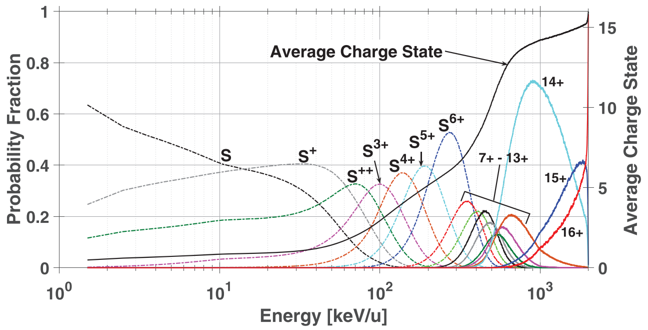

Figure 3. Sulfur charge state distribution as a function of ion energy. The high charge state peaks have dramatically shifted to lower energies than previous models produced. Ozak et al. (2010) had the peaks of S^{6+} and S^{14+} at ~500 keV/u and ~2.2 MeV/u, respectively. Due to the use of newly developed SIM cross sections, the peaks have now shifted down to energies of ~275 and ~900 keV/u, respectively.

At angles between 0° and 80°, the Chapman function has been approximated to

$$Ch(0^\circ \leq \theta \leq 80^\circ, z_0) \approx \sec(\theta), \tag{5}$$

and since this approximation tends toward infinity for $\theta = 90^\circ$, for this case, we then use

$$Ch(\frac{\pi}{2}, z_0) = \sqrt{\frac{R_J}{H(z_0)}\frac{\pi}{2}}, \tag{6}$$

where R_J is the Jovian radii of 71,492 km and $H(z_0)$ is the scale height at altitude z_0. The spectrum intensity, $4\pi I(\lambda)$ can then be calculated as

$$4\pi I(\lambda) = \int_{z_0}^{\infty} P(\lambda, z) e^{-\tau(\lambda, z_0)} \mathrm{d}z, \tag{7}$$

where $P(\lambda, z)$ is the production rate of X-ray emission as a function of wavelength, λ, and altitude, z. z_0 is the deepest altitude that is reached by the ion beam before all of its energy is deposited into the atmosphere, and $\tau(\lambda, z_0)$ is the aforementioned optical depth.

$P(\lambda, z)$ integrated over every value of λ is equal to the ion production rate, $P(z)$, and can be calculated for a given ion charge state. Therefore, to determine the production rate as a function of wavelength, there are a couple of things to note before building approximate synthetic spectra.

2.5. Approximated Synthetic X-Ray Spectra

An X-ray can be emitted through either the ion gaining an electron (what we refer to as a charge transfer or charge exchange collision) or the excitation of the ion (called direct excitation). Both of these scenarios result in one or more electrons in an excited state followed by emission of a photon as the electron(s) cascade down to a lower energy state. Although there are many charge transfer and projectile excitation processes, we only allow three of each type to ultimately result in the emission of a photon: TI, SC, and SC+SS for charge exchange and SI+SPEX, DI+SPEX, and TEX+SPEX for direct excitation. Any collisions that result in more than one electron being in an excited state at a given time, whether it be through charge exchange, projectile excitation, or a combination of the two (e.g., DC or SC+SPEX collisions), we consider it much more likely for the Auger effect (the energy being given to an ejected electron) to take place than the emission of a photon.

Due to the lack of published X-ray emission cascade models and given the distribution of electronic excitation given by our ion-precipitation model, we have adopted synthetic spectra resulting from charge transfer for O and S ions by Hui et al. (2010). These spectra are available only at ion energies somewhat above those needed here, owing to the shift of the charge state distributions to lower energies from use of the SIM processes model. Using the data available from Hui et al. (2010), we have produced approximated spectra versus number of photons/ion which we have renormalized for each charge state to the total number of photons/charge state. We then multiplied the ion production from charge exchange produced by our model, $P(z)$, by the normalized emission lines to generate $P(\lambda, z)$.

We do not have any state-selective excitation emission spectra of oxygen and sulfur for direct excitation; instead, we apply an approximation to the charge exchange emission lines we do have available.

In general, energy levels reached by excitation of the projectile ion will be predominantly to lower levels than those from charge transfer. Charge transfer proceeds to states with principal quantum number n peaked at $\approx q^{3/4}$ (Grozdanov & Janev, 1978; Olson, 1981), with a distribution below and above this, falling off at high quantum number as $1/n^3$ (Oppenheimer, 1928; Schultz et al., 2010). In contrast, excitation proceeds dominantly to the next highest n level and rapidly falls off for higher n. (Note: Another consideration is forbidden excitation transitions for each charge state; however, that requires a much more in-depth study of the situation beyond the scope of the research presented here.) Thus, we have approximated the excitation to the next highest n level as 80–85%, the possibility of excitation of two n levels as 15%, and to a third higher excitation level as 0–5%.

To do this, we take the two or three most common emission lines, at lower photon energies, from the charge exchange synthetic spectra provided by Hui et al. (2010) and distribute the direct excitation emission in the following way

$$\sum_{i=1}^{2,3} \frac{hc}{\lambda_i} f_i = E, \tag{8}$$

where h is Planck's constant, c is the speed of light, and λ_i is the wavelength of the most likely emission line or group of emission lines. If there is a group of emission lines with similar wavelengths ($\Delta\lambda \approx 10$ eV), the emission is distributed evenly among each wavelength because in this simple approximation, we do not know the exact state-selective excitation transitions, and forbidden excitation states have not been considered. f_i is the distribution of X-ray production given to each wavelength. If only two lines (or groups of lines)

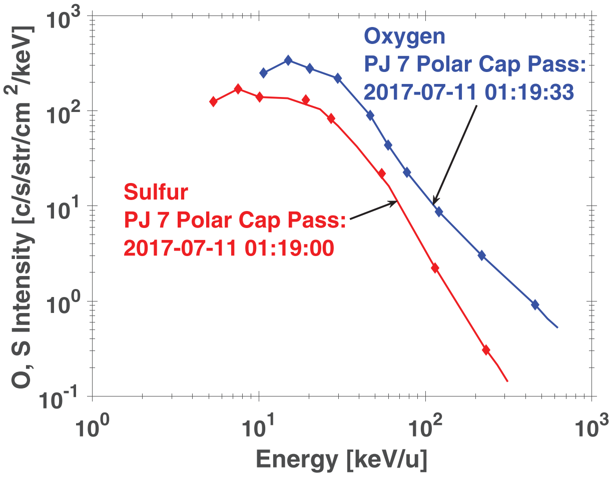

Figure 4. Downward precipitating oxygen and sulfur flux measurements from JEDI on the Juno spacecraft during Perijove 7. The points marked with a diamond are the actual JEDI measurements. The lines represent the interpolation of the data that we applied to the measurements. Note the power law distribution seen in both species; however, oxygen appears to have an extended high energy tail when compared with sulfur.

are considered, then $f_1 = 0.85$ and $f_2 = 0.15$; for three, $f_1 = 0.80$, $f_2 = 0.15$, and $f_3 = 0.05$. E is the total photon energy from emission.

To ensure this approximation is not violating conservation of energy, if the emitted photon energy is greater than the energy loss for SPEX, $E > \Delta E$, where ΔE is the energy loss for SPEX at a given ion energy and charge state shown in Schultz et al. (2019), then the emission given in equation (8) is renormalized to conserve energy,

$$\sum_{n=1}^{2,3} \frac{hc}{\lambda_n} f_n \epsilon = E, \tag{9}$$

where $\epsilon = \Delta E/E$. If $E < \Delta E$, then we keep the distribution as is and assume the energy difference is due to emission from lower energy photons not considered in the X-ray spectrum and X-ray inefficiencies in emission from the way the electrons cascade through the electron orbitals.

To produce a more realistic approximate synthetic spectrum comparable with observation that an X-ray observatory would detect, we apply a normalized Gaussian distribution to each data point to simulate instrumental response functions, recovering a new intensity:

$$4\pi I'(\lambda) = \sum_{\lambda_\mu} \frac{1}{\sqrt{2\pi\sigma^2}} I(\lambda) e^{-\frac{(\lambda-\lambda_\mu)^2}{2\sigma^2}}, \tag{10}$$

where λ is now the full spectrum (in eV) which we allow to range from 100 to 3,500 eV. λ_μ is the wavelength of each emission line, and σ^2 is the variance, where $\sigma = 20$ eV. A careful data-model comparison requires instrument response functions (e.g., for CXO or XMM-Newton).

2.6. Juno Data

With recent measurements from JEDI (Mauk et al., 2017) on the Juno spacecraft, we have obtained heavy ion flux measurements above Jupiter's polar caps indicating both oxygen and sulfur precipitation (Clark, Mauk, Haggerty, et al., 2017; Clark, Mauk, Paranicas, et al., 2017; Haggerty et al., 2017). We input these measurements into our model and produce expected observables for a given flux. For this study, we use downward precipitating heavy ion measurements from a northern auroral pass during Perijove (PJ) 7 on 11 July 2017, displayed in Figure 4. These measurements are taken during a time when Juno's magnetic footprint is leaving the polar cap and crossing equatorward over the main auroral oval.

Renormalization and interpolation of all of the data is necessary to make the flux compatible with the ion precipitation model. The renormalization requires multiplying the measured intensity by the JEDI energy bin widths (Mauk et al., 2017) and 2π to obtain a flux in ions/cm^2/s. The first three energy bins (170.7, 240.2,

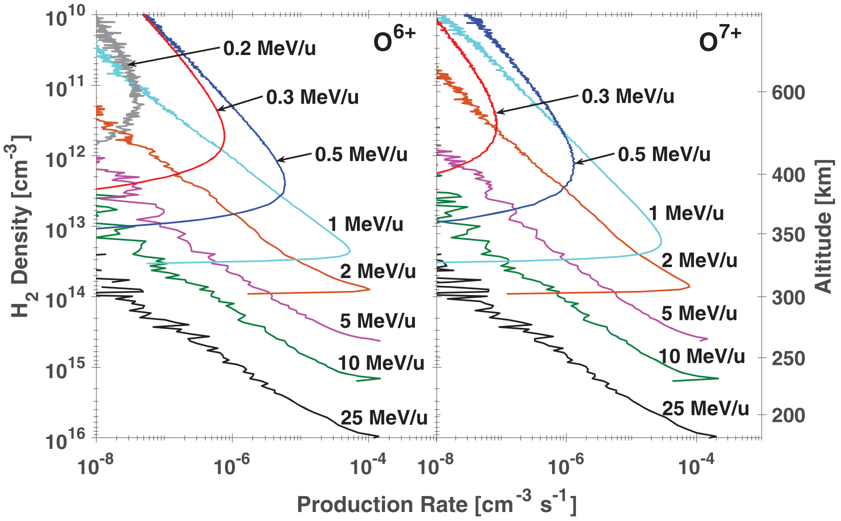

Figure 5. The O^{6+} and O^{7+} production rates from TI, SC, and SC+SS versus H_2 density and altitude for various incident ion energies (E = 0.2, 0.3, 0.5, 1.0, 2.0, 5.0, 10.0, and 25.0 MeV/u). The production rates have been normalized to a single incident ion/cm^2/s.

and 323.6 keV) on the JEDI instrument are unable to distinguish between oxygen and sulfur, but fortunately, these low energy bins will not contribute to X-ray production. We then use a simple linear interpolation to give the data finer resolution so the results are smoother, although it has no effect on the total X-ray production. These flux measurements are then used as an input ion flux into our model, or more simply, one can multiply the output from various monoenergetic runs (which are normalized to an input of 1 ion/cm^2/s) by the renormalized flux given by JEDI.

It is important to note that although the low energy bins are unable to distinguish between oxygen and sulfur, the higher energy bins of JEDI make separate oxygen and sulfur measurements, and in the case presented, oxygen happens to be more abundant. This is not necessarily a typical measurement, and as suggested by X-ray observation, we generally expect sulfur to produce higher concentrations of X-ray emission. Data have indicated that the sulfur to oxygen (S:O) ratio varies between measurements (Delamere et al., 2005; Dougherty et al., 2017; Kim et al., 2019) which needs to be considered when comparing approximated synthetic X-ray spectra with that from observation. Figure 4 has an S:O ratio of about 0.8 which is a midrange ratio presented by Radioti et al. (2005, 2006), where the S:O ratio is shown to vary between 0.3 and 1.2.

Jupiter's X-ray aurora is known to be highly time variable. The X-ray aurora pulses/flares on timescales of a few minutes, while the power output from the aurora can vary by a factor of a few from rotation to rotation (0.5–2 GW), and the spectrum is known to change significantly on similar timescales (e.g., Branduardi-Raymont et al., 2007; Elsner et al., 2005; Hui et al., 2010). The spatial location of the emission may also vary across the auroral zone (Dunn et al., 2017; Gladstone et al., 2002; Jackman et al., 2018), with some suggestion that sulfur X-ray lines may be brighter at lower auroral latitudes (Dunn et al., 2016).

3. Results

3.1. Ion Production Rates

When referring to ion production rates here, we are only focusing on production from charge transfer collisions, that is, $X^q \rightarrow X^{q-1}$, and not stripping collisions, which change the charge state in the opposite direction. We will only consider the ion production rate from the collisions that produce photons, that is, mainly TI, SC, and SC+SS. Furthermore, the ion production rate as a function of altitude, $P(z)$, can be calculated outright for a product ion species, i, (e.g., O^{7+} or S^{8+}) as follows:

$$P(z) = n(z)[\sigma^i_{q,q-1}(E(z))]\phi^i_q \Phi^i, \tag{11}$$

where $n(z)$ is the neutral atmosphere density of H_2, $\sigma^i_{q,q-1}(E(z))$ denotes the charge transfer cross sections for species i with energy E at altitude z, ϕ^i_q is the equilibrium fraction given in equations (2) and (3), and Φ^i represents the total flux of the initial ion beam. However, our model uses a Monte Carlo method that tracks

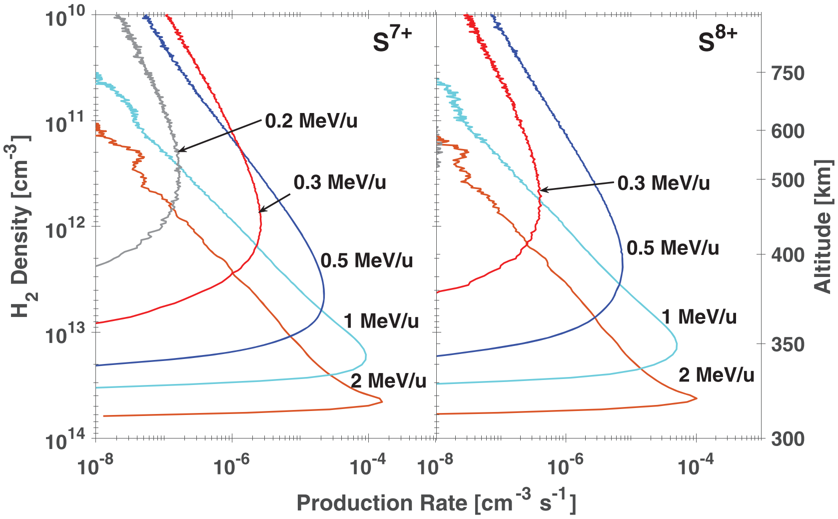

Figure 6. The S^{7+} and S^{8+} production rates from TI, SC, and SC+SS versus H_2 density and altitude for various incident ion energies (E = 0.2, 0.3, 0.5, 1.0, and 2.0 MeV/u). The production rates have been normalized to a single incident ion/cm^2/s.

each ion individually and counts each charge exchange collision that occurs for a given charge state. These collisions are tracked through a set of altitude bins with a given input of ~20,000 incident ions, and then the production rate is normalized to an input of 1 ion/cm^2/s. The production rates as a function of H_2 density and altitude for O^{6+} and O^{7+} are shown in Figure 5. For sulfur, Figure 6 shows the S^{7+} and S^{8+} charge transfer production rates. It is to be emphasized that these production rates only include charge exchange from the three collisional processes discussed in section 2.5, that is, TI, SC, and SC+SS; although other processes can contribute to lowering the overall charge state without emitting a photon (e.g., the Auger process). The altitude integrated production rates for every charge state and various initial ion energies can be found in Appendices A and B (Tables A1, A2, B1, and B2), including the production rate of directly excited ions. It is worth noting that, for sulfur, these results use preliminary data and may be subject to revision.

It is evident from Figures 5 and 6 that the production rate of X-ray producing charge states from charge exchange collisions, O^{6+} and S^{7+}, is obtained with energies as low as 200 keV/u, which is well within the range of ion energies measured by Juno above the polar caps (Clark, Mauk, Haggerty, et al., 2017; Clark, Mauk, Paranicas, et al., 2017; Haggerty et al., 2017).

3.2. X-Ray Efficiencies

The emitted photon flux is determined by using the production rates, shown in Figures 5 and 6 and equation (7), where 4π is included to convert the intensity units from cm^{-2} s^{-1} sr^{-1} to cm^{-2} s^{-1}. X-ray emission efficiency is a way of quantifying how many photons are emitted given an incident ion energy and is found by dividing $4\pi I$ by the initial energy of the monoenergetic ion beam. Table 1 shows the combined X-ray efficiencies from both charge exchange and direct excitation emission given an incident ion energy, at various viewing angles, using both Atmospheres 1 and 2, and with an input of 1 ion/cm^2/s. The same is also shown in Figures 7 and 8. Given the approximations noted above to infer the electron state populations from charge transfer and projectile excitation, the full set of efficiencies for every X-ray emitting charge state at each energy and three different viewing angles plus a no opacity case can be found in Appendices A and B, Tables A3-A6 and Tables B3-B10.

The most efficient X-ray emission for O^{6+} is with an incident ion energy of ~600 keV/u for both atmospheres, ~1 MeV/u for O^{7+}, ~500 keV/u S^{8+}, and ~600 keV/u for S^{9+}. The well-mixed atmosphere has minimal effects on emission from low energy ion precipitation because the ions are not precipitating deeply enough for the large column density to have much of an impact on the X-rays. As one would expect, the viewing angle of 90° greatly reduces emission for high energy ion precipitation when comparing with X-rays that propagate directly up and out of the atmosphere at 0°. This is even more true for X-ray production from sulfur which is the overall most efficient X-ray producer (i.e., S^{8+} at 500 keV/u) with a viewing angle of 0°, but the efficiency is reduced by nearly 60% (for Atmosphere 1) when the viewing angle changes to 90°, whereas O^{6+} is only

Table 1

The X-ray Efficiency ($[cm^2 sec]^{-1}[keV/u]^{-1}$) of Outgoing Photons as a Function of Initial Ion Energy Including Opacity Effects From a Single Incident ion/cm^2/s With an Isotropic Downward Distribution of Pitch Angles

Energy	0°				90°			
(keV/u)	O^{6+}	O^{7+}	S^{8+}	S^{9+}	O^{6+}	O^{7+}	S^{8+}	S^{9+}
Atmosphere 1 (Original atmosphere)								
200	0.0141	0.0005	0.0023	0.0001	0.0139	0.0005	0.0019	0.0001
300	0.1195	0.0106	0.0514	0.0085	0.1165	0.0104	0.0365	0.0072
400	0.2008	0.0317	0.2093	0.0745	0.1901	0.0309	0.1195	0.0563
500	0.2669	0.0735	0.3208	0.1882	0.2358	0.0701	0.1327	0.1206
600	0.2884	0.1206	0.3020	0.2145	0.2235	0.1107	0.0772	0.1022
700	0.2787	0.1578	0.2557	0.1924	0.1760	0.1357	0.0370	0.0589
800	0.2573	0.1810	0.2169	0.1663	0.1240	0.1409	0.0185	0.0300
900	0.2333	0.1911	0.1858	0.1443	0.0827	0.1303	0.0106	0.0157
1,000	0.2105	0.1918	0.1608	0.1265	0.0551	0.1118	0.0069	0.0093
2,000	0.0954	0.1244	0.0527	0.0474	0.0029	0.0128	0.0009	0.0009
Atmosphere 2 (Well-mixed atmosphere)								
200	0.0140	0.0005	0.0022	0.0001	0.0134	0.0005	0.0015	0.0001
300	0.1192	0.0106	0.0507	0.0084	0.1068	0.0100	0.0267	0.0057
400	0.2000	0.0317	0.2048	0.0736	0.1643	0.0289	0.0799	0.0418
500	0.2653	0.0733	0.3113	0.1849	0.1867	0.0633	0.0792	0.0817
600	0.2861	0.1201	0.2904	0.2093	0.1606	0.0954	0.0397	0.0600
700	0.2761	0.1570	0.2441	0.1864	0.1156	0.1111	0.0170	0.0297
800	0.2545	0.1799	0.2060	0.1602	0.0756	0.1096	0.0084	0.0138
900	0.2307	0.1898	0.1760	0.1386	0.0478	0.0967	0.0050	0.0072
1,000	0.2080	0.1904	0.1521	0.1212	0.0311	0.0802	0.0033	0.0044
2,000	0.0942	0.1234	0.0498	0.0453	0.0017	0.0087	0.0006	0.0006

Note. The viewing angles of 0° and 90° are displayed for both Atmospheres 1 and 2. The efficiencies shown here include X-ray production from both charge exchange and direct excitation collisions.

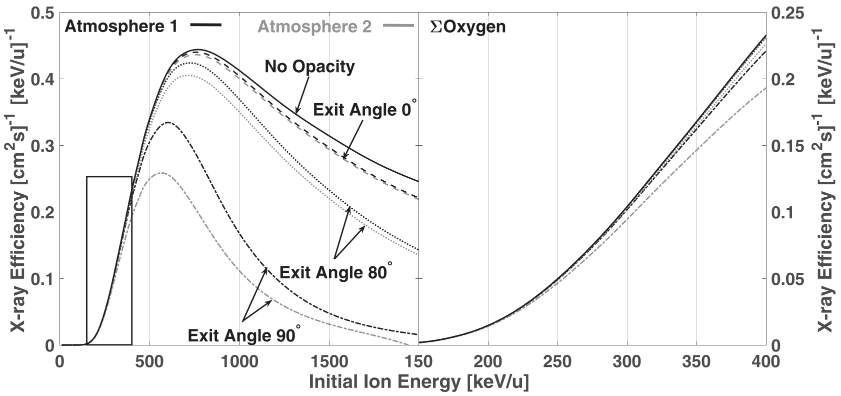

Figure 7. The entire outgoing X-ray flux efficiency for all X-ray producing oxygen charge states as a function of initial ion energy from a single incident ion/cm^2/s with an isotropic downward distribution of pitch angles. The condition of no opacity is shown by the solid line, an exit angle of 0° is represented by the dashed line, an exit angle of 80° by the dotted line, and an exit angle of 90° by the dash-dot line. Atmosphere 1 is in black, and Atmosphere 2 is in gray. Every exit angle is with respect to the Jovian spin axis. The figure on the right is a magnified portion of the figure on the left (represented by the black rectangle), used to emphasize the efficiencies of ions in the energy range of JEDI measurements.

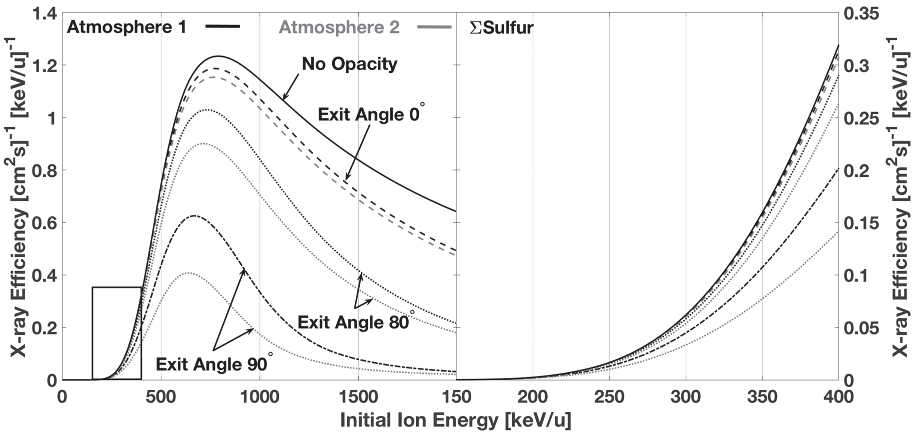

Figure 8. The entire outgoing X-ray flux efficiency for all X-ray producing sulfur charge states as a function of initial ion energy from a single incident ion/cm^2/s with an isotropic downward distribution of pitch angles. The condition of no opacity is shown by the solid line, an exit angle of 0 is represented by the dashed line, an exit angle of 80° by the dotted line, and an exit angle of 90° by the dash-dot line. Atmosphere 1 is in black, and Atmosphere 2 is in gray. Every exit angle is with respect to the Jovian spin axis. The figure on the right is a magnified portion of the figure on the left (represented by the black rectangle), used to emphasize the efficiencies of ions in the energy range of JEDI measurements.

reduced by about 23% (for Atmosphere 1) making it the most efficient emitter at 90°. This is an important effect to consider when looking at fluxes from Earth-orbit-based X-ray observations, which are generally taken at a steep viewing angle, especially for the southern aurora.

Ozak et al. (2010) reported that the most efficient X-ray emission for O^{6+}, O^{7+}, and S^{8+} was for incident ions with energies of 1.5, 2.5, and 1 MeV/u and efficiency values of ~0.009, ~0.003, and ~0.015, respectively. These energies are 2–3 times higher than what JEDI typically observes. But our revised model with the SIM cross sections indicates that for O^{6+}, O^{7+}, and S^{8+}, the most efficient X-ray emissions occur at energies of 600 keV/u, 1 MeV/u, and 500 keV/u with efficiencies of 0.29, 0.19, and 0.32, respectively (from Table 1, Atmosphere 1, 0° viewing angle). Two major contributions account for such a great difference in X-ray efficiencies. First, with the more complete treatment of the fundamental atomic collision processes, it requires much less energy than inferred in the previous models to strip both oxygen and sulfur ions to a high, X-ray producing charge state, allowing X-rays to be created at much lower energies than previously thought. Second, we are depositing much more energy higher up in the atmosphere due to the increase in stopping power shown by Schultz et al. (2019), ultimately generating X-rays higher in the atmosphere than previously modeled, making them less susceptible to opacity effects even when considering an upper-limit, highly mixed atmosphere.

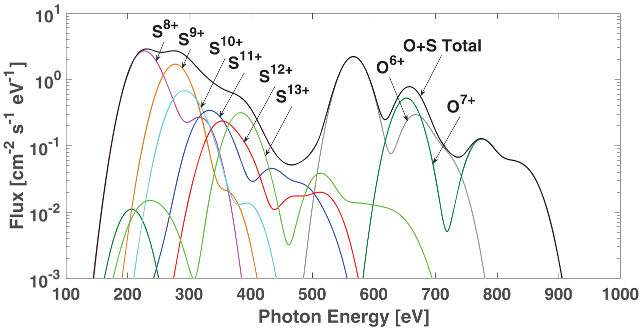

Figure 9. Approximated synthetic X-ray spectra showing the contribution from each charge state. This spectrum includes emission from both charge exchange and direct excitation collisions considering no opacity effects from an incident ion beam of 500 keV/u with an input is 1 ion/cm^2/s for both species. Not shown is the emission from S^{14+} which peaks at ~2,450 eV with an intensity several orders of magnitude lower than the more prominent emission lines.

There are several useful ways to interpret X-ray efficiencies. Because the efficiencies are calculated with an input of 1 ion/cm^2/s, one can view each efficiency as the number of X-ray photons emitted given an initial ion energy. That is to say, if a single oxygen ion with an energy of 300 keV/u is precipitating, then it is expected that ~0.1 photons/cm^2/s/(keV/u) × 300 keV/u ≈ 30 photons/cm^2/s will be emitted. Therefore, 1 oxygen ion/cm^2/s at 300 keV/u will produce about 30 photons/cm^2/s or 1 ion/s precipitating results in 30 photons/s. This is an extremely quick estimate that can be made when trying to interpret the emission from a measured JEDI ion flux and is useful if considering an X-ray instrument for a future mission to Jupiter.

Another practical application of the X-ray efficiencies is to calculate total X-ray power emission for a given initial ion energy. For example, we have just calculated that 1 oxygen ion/s at 300 keV/u will produce 30 photons/s. The average emitted photon energy associated with oxygen is 600 eV (see section 3.3). The power out is then 30 photons/s × 600 eV ×

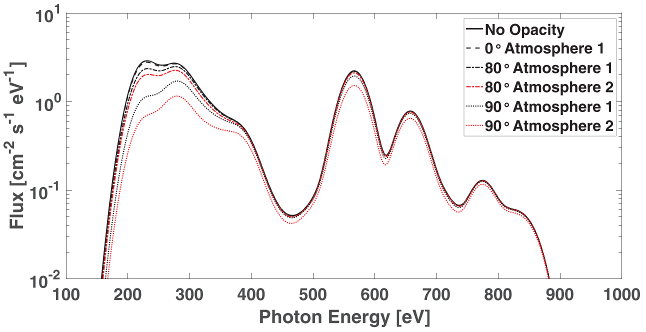

Figure 10. Approximated synthetic X-ray spectra with opacity effects at three viewing angles through an atmosphere with a deep, originally considered homopause (Atmosphere 1) and an atmosphere that is well-mixed through the top of the atmosphere (Atmosphere 2), what we consider an upper limit to opacity effects. Initial ion energies are 500 keV/u for both oxygen and sulfur precipitation and the input is 1 ion/cm^2/s for both species. Photon energies below about 400 eV are shown to be much more affected by the opacity than higher photon energies.

1.6×10^{-9} J/eV $\approx 3 \times 10^{-15}$ J/s or 3×10^{-15} W. Thus, given an ion flux, one can approximate the total power output from the precipitating ions.

Finally, given an ion flux, one can estimate the power output from the entirety of the polar cap or a defined area that Juno has flown over, while an X-ray observation has been made simultaneously. If photons/cm^2/s is calculated, either through the aforementioned method or as a direct result output from our model with a variety of initial ion energies, then finding the power/cm^2/s is a matter of combining the two previous methods. That is, (photons/cm^2/s) × (average photon energy [eV]) × (1.6×10^{-19} J/eV) results in W/cm^2. Now, if the area of the measurement is known or deduced by geometry, multiplying power/cm^2 by the area will result in the total power for that area, which can be directly compared to an observed total X-ray power (or luminosity).

3.3. X-Ray Spectra

Distributing the X-ray intensity into individual lines, as given by the approximate treatment of the synthetic spectra as described in section 2.5, we can provide X-ray spectra. Figure 9 shows the total X-ray emission for a single oxygen plus a single sulfur ion (sulfur to oxygen ratio of 1:1), both with incident energies of 500 keV/u. The emission lines have been distributed with a normalized Gaussian and $\sigma = 20$ eV, simulating instrument response functions (discussed in section 2.5). The emission is plotted by charge state to show where in the spectrum, each emission line contributes the most, that is, sulfur dominates at photon energies between 150 and 500 eV, while oxygen is prominent between 500 and 900 eV. This particular spectrum (Figure 9) accounts for no opacity effects, and we have included emission from both charge exchange and direct excitation collisions. The emission from S^{14+} has two peaks at ~430 and ~2,450 eV, but the latter is multiple orders of magnitude below the rest of the emission and would therefore be much fainter than the dominant lines in Figure 9.

Figure 10 is the same total emission from Figure 9 (black line) with opacity effects applied from both Atmospheres 1 and 2 at three different viewing angles. It is apparent that the lower energy X-ray emissions from sulfur are much more affected by opacity than those from oxygen, which was indicated by the X-ray efficiencies in Table 1. This is due to the relatively large photo-absorption cross sections at longer wavelengths, shown by Cravens et al. (2006). The relative absorption is useful when comparing emissions from the northern and southern aurorae, because the southern aurora is generally observed at a much steeper viewing angle than the northern aurora.

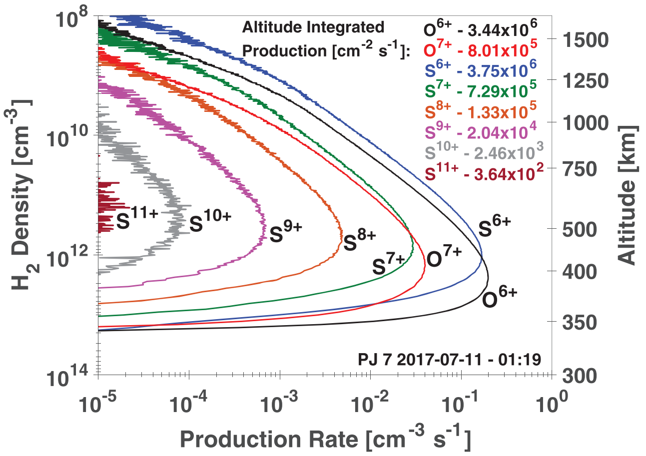

Figure 11. Ion production rate from X-ray producing charge exchange collisions combined with X-ray producing direct excitation collisions of each ion charge state versus H_2 density and altitude from Juno's PJ 7 pass. Also included is the altitude integrated production rate of each charge state displayed. It is evident from the charge states obtained that X-rays will be produced.

It is also important to note how little X-ray absorption occurs at this energy of 500 keV/u, even for Atmosphere 2. A 500 keV/u oxygen ion (total energy of 8 MeV) is nearing the upper energy limit of the JEDI instrument of 10 MeV (Mauk et al., 2017) and a 500 keV/u sulfur ion (16 MeV) is above that limit. This suggests that precipitation of ions with energies within the JEDI limits will have X-ray emission that will escape without undergoing large opacity effects and should be detectable, even if a very well-mixed atmosphere is present. Due to the new SIM cross sections precluding the X-ray producing ions from precipitating deep into the atmosphere, these results are much different than those presented by Ozak et al. (2010), which show a reduction in sulfur emission by nearly 2 orders of magnitude when considering a 90° viewing angle.

3.4. Inputting JEDI Measurements

Finally, we input the JEDI flux measurements, displayed in Figure 4, into our model and are able to determine ion production rates, direct excitation rates, and an expected X-ray spectrum. In the results presented using JEDI measurements, we only consider Atmosphere 1, the original atmosphere in Figure 1 with a well-defined homopause. Displayed in Figure 11 are the ion production rates from X-ray producing charge exchange collisions (TI, SC, SC+SS) combined with the production rates from X-ray

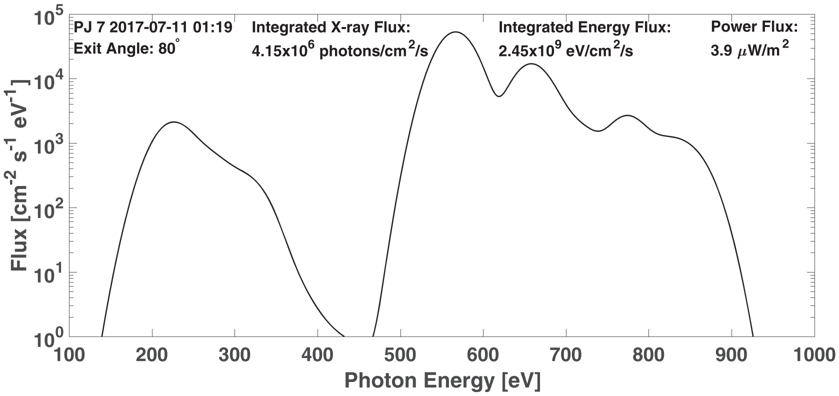

Figure 12. Predicted X-ray spectrum from JEDI's ion flux measurements during the PJ 7 polar cap pass in 2017. This spectrum assumes an opacity effect with an exit angle of 80° through Atmosphere 1. It appears emission from oxygen is the most prominent source of X-rays associated with this flux measurement, which may have been anticipated from the JEDI data taken at this time, but is likely not always the case.

producing direct excitation collisions (SI+SPEX, DI+SPEX, and TEX+SPEX) associated with the PJ 7 ion flux measurements. This demonstrates that the ions seen during this pass are of sufficient energy to reach X-ray producing charge states. It is also evident that X-ray emitting ions do not precipitate deeply enough to go much below the homopause, indicating that absorption will have minimal effects.

Displayed in Figure 12 is the X-ray spectrum we predict using a JEDI measurement of an instant of a particularly high ion flux during PJ 7 (Figure 4), included is X-ray production from both charge exchange and direct excitation collisions. This particular spectrum considers opacity effects with a photon exit angle of 80°, which we assume to be a common viewing angle from Earth-orbit-based observations, although opacity effects make little difference on the X-ray emission from ions with this low of initial energy. (Note: When comparing an 80° exit angle to a 90° exit angle, the total emitted flux from oxygen emission was only reduced by 5.4% for the 90° case, while emission from sulfur was diminished by 15%.)

3.5. Comparing Simulated and Observed X-Ray Spectra

The XMM-Newton Observatory observed Jupiter continuously from 19:29 on 10 July to 09:38 on 12 July 2017. Part of this observation was simultaneous with the Juno JEDI ion measurements presented in section 3.4 and Figure 4. Unfortunately, since Jupiter's aurorae rotate with the planet, the Northern X-ray aurora was not in view from Earth precisely when Juno conducted in situ particle measurements in the X-ray auroral region but was observable 2 hr prior to this and 1 hr after (see supporting information for comparisons of Juno flight with auroral viewing). Here, we compare the simulated Northern auroral X-ray spectrum from the Juno JEDI in situ measurements with contemporaneous observed X-ray auroral spectrum.

We extracted and calibrated the observed X-ray spectrum from Jupiter's Northern aurora during the two intervals (19:29–21:30 on 10 July and 01:00–06:00 on 11 July [UT]) that bracketed the Juno JEDI ion measurements (section 3.4 and Figures 4 and 12). One-way light travel from Jupiter to XMM-Newton between 10 and 12 July 2017 was 45 min. The northern aurora rotated out of view for XMM-Newton at ~21:30 UT (light emitted from Jupiter at 20:45) and came back into view at ~01:50 (light emitted from Jupiter at 01:05). During this interval, there was not perfect coincidence of Juno measuring the X-ray emitting region and the subsequent X-rays being observed at Earth. We found that the X-ray aurora in this interval was relatively dim (~50% of the power output observed in the subsequent two auroral observations on the 11 and 12 July, see supporting information).

We took the simulated X-ray photon fluxes emitted from the in situ ion flux measurements at a 60° viewing angle to represent the latitudinal location of the observed northern X-ray emissions (e.g., see Dunn et al., 2017; Gladstone et al., 2002). We multiplied these photon fluxes per cm^2 by the area of a typical dim X-ray auroral region (e.g., time-binned X-ray projections in Dunn et al., 2016) to attain a total flux of photons from the aurora. We then scaled these auroral photon fluxes by $4\pi r^2$ to account for their dispersion between Jupiter and XMM-Newton. Having calculated fluxes arriving at XMM, we applied XMM-Newton's time-dependent instrument responses on 10 July (XMM-Newton calibration, response matrices, and ancillary response files) to the simulated photon fluxes. This provided a simulated X-ray spectrum for what would be detected by XMM-Newton on 10–11 July 2017. Finally, we compared the simulated and observed spectra by calculating the reduced Chi-Squared between the two.

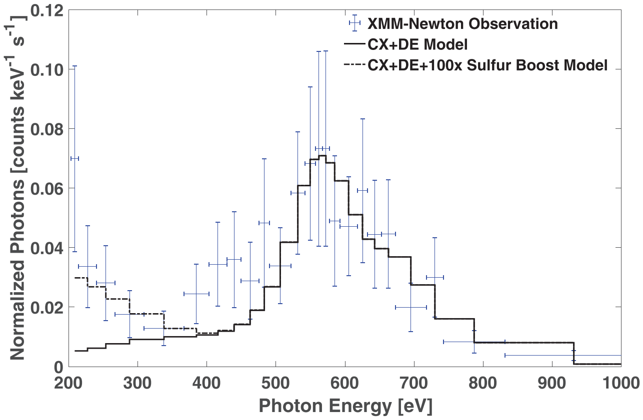

Figure 13. An XMM-Newton EPIC-pn observation of Jupiter's Northern X-ray Auroral spectrum from 19:29 to 21:30 on 10 July 2017 (blue crosses) binned to ensure at least 5 counts per energy channel. Overlaid on the observational data is the simulated photon fluxes from Figure 12 that has been normalized using the XMM-Newton EPIC-pn instrument response to produce a simulated X-ray spectrum (black solid line, S:O ratio of 0.8) and a second, sulfur boost of 100×, X-ray spectrum (black dash-dotted line). This assumes an X-ray auroral region of 2.5° × 7.5° (a surface area of ~2×10^{17} cm^2) System III latitude-longitude, demonstrating a good morphological fit to the spectra based on the shape of emission.

Figure 13 shows the comparison between the simulated spectrum (black lines) and the observed data from 19:29 to 21:30 on 10 July 2017 (blue crosses). The results were similar for both intervals (see supporting information). The simulated oxygen emission between 0.5 and 0.9 keV is an excellent fit to the observed spectrum for both intervals producing a reduced χ^2 of 1.3–1.5 (Table 2). However, below 0.5 keV, the simulated sulfur photon fluxes do not well reproduce the observed emission, which leads to a reduced χ^2 of 4–5 for the overall spectrum from both intervals (Table 2). Consequently, we investigate a "boosted" sulfur model (black dash-dotted line in Figure 13) to determine how much sulfur emission is necessary to reproduce the observed spectrum. A sulfur boost of 100× is needed to fit the emission measured by XMM-Newton; this is concerning due to the luminosity associated with this large of a boost (~7 GW, which is notably higher than typical X-ray observations, discussed in section 3.6). This lower energy spectrum could also be fit well with a bremsstrahlung continuum, but this does not resolve the high luminosity issue. Alternatively, this discrepancy may be a result of the poor effective area for the XMM-Newton EPIC-pn instrument below 0.3 keV. Ultimately, more input data (JEDI measurements) and XMM-Newton observation comparisons are required for greater statistical significance; because, as Figure 4 indicates, the high energy tail of the sulfur spectrum falls off more rapidly than that of oxygen, which is likely not always the case. It is to be considered that the sulfur data are preliminary; however, we do not expect any substantial changes in the sulfur cross sections to resolve the disagreement presented here.

The spectral morphology in the <0.3 keV X-ray energy range appears line-like but could also be fitted well by a large flux of photons from a low energy bremsstrahlung continuum (see supporting information for details). The discrepancy between 0.2 and 0.5 keV also appears between Figures 10 and 12. Figure 4 shows that there was an S:O ratio of 0.8 during this interval. Radioti et al., 2005 (2005, 2006) showed that the S:O ratio in the magnetosphere varies from 0.3 to 1.2, so this ratio appears to be a typical measurement. However, Figures 9 and 10 suggest that this may have been an intermittent relatively low ratio, showing that an S:O ratio of 1:1 produces a spectrum that morphologically is much closer to the observed X-ray spectrum. Thus, a secondary process (aside from sulfur precipitation) should likely be considered to contribute to that part of the spectrum. The X-ray aurora is also known to be highly time variable on scales of tens of minutes to hours (e.g., Dunn et al., 2017), so it may be that the conditions changed between the PJ pass through the X-ray auroral zone and the auroral emissions that were observed.

To account for the low predicted sulfur emission, we briefly consider a bremsstrahlung component to either replicate a forest of sulfur lines between 0.2 and 0.5 keV or to reproduce a high energy bremsstrahlung

Table 2
XMM-Newton Northern Auroral Observations With Auroral Models

Observation time	Model	Reduced χ^2 fits	Auroral power observed (mW/m^2)	Auroral power simulated (mW/m^2)
10 July 19:29–21:30	CX+DE	5	1×10^{-13}	3×10^{-14}
10 July 19:29–21:30	CX+DE+ Bremsstrahlung	1.3	1×10^{-13}	7×10^{-14}
11 July 01:00–05:30	CX+DE	4	8×10^{-14}	3×10^{-14}
11 July 01:00–05:30	CX+DE+ Bremsstrahlung	1.5	8×10^{-14}	5×10^{-14}

component (above 0.9 keV), which is sometimes present in the X-ray aurora from energetic electrons (e.g., Branduardi-Raymont et al., 2004, 2008). Including these bremsstrahlung components was found to improve the fits (Table 2). Much of Jupiter's ultraviolet aurora is known to be produced by electron precipitation, and a bremmstrahlung continuum has been found to provide an excellent fit to the X-ray emission above 2 keV in Branduardi-Raymont et al. (2004). But in this work we concentrate on the spectral line emission from ion precipitation. Figures for these fits can be found in the supporting information alongside comparisons of the Juno flight path with the X-ray auroral emission region and X-ray light curves from this interval.

In summary, our models produce excellent predictions for the observed X-ray emission from oxygen precipitation into the atmosphere, if the X-ray auroral zone covers a region of between 5° to 10° by 5° to 10° in System III latitude-longitude. There are still open questions about whether the sulfur emission is underestimated because of time-varying changes in the ion precipitation or because of some, as yet unidentified, differences between the treatment of oxygen and sulfur behavior. To identify this, it will require additional XMM-Newton observations coincident with Juno measurements at PJ. These observations are planned for September 2019.

3.6. X-Ray Luminosity

Can heavy ion precipitation produce *enough* X-ray emission to explain the total observational soft X-ray luminosity of 1–2 GW (Elsner et al., 2005; Gladstone et al., 2002) A quick estimate confirms that the new model can produce such luminosity. The X-ray emission our model produces when the JEDI ion flux measurement shown in Figure 4 are input is $\sim 4 \times 10^6$ photons/cm^2/s. This is the sum of all oxygen and sulfur X-ray emission from both charge exchange and direct excitation with an exit angle of 80° from the original atmosphere. Integrating the emission in Figure 12 results in $\sim 2.5 \times 10^9$ eV/cm^2/s. Converting this to W/cm^2 by multiplying by a factor of 1.6×10^{-19} J/eV yields a power output of 4×10^{-9} W/cm^2. Now, the total area of X-ray emission on the Jovian polar cap can be assumed to come from within a latitude of ~5°. This gives an area of $2\pi R_J^2(1\text{-}\cos\theta) \approx 10^{18}$ cm^2 (Jovian radii $[R_J] = 71{,}492$ km). The 4×10^{-9} W/cm^2 $\times\, 10^{18}$ cm^2 $= 4 \times 10^9$ W or 4 GW. It appears, based on this quick, “back of the envelope” calculation, that we can now account for the entirety of the output power of the X-rays. Of course, the area of emission needs to be greatly constrained, and this was for a single, instantaneous JEDI measurement that observed a high ion flux, but this shows that it is now feasible the ion flux measurements at Jupiter are responsible for the X-ray emission. For further discussion on using the data provided in this manuscript to calculate X-ray emission, efficiency, and power, refer to Appendix C.

4. Discussion and Conclusions

Spectral lines from precipitating ions have been known to dominate Jupiter's X-ray aurora since the launch of XMM-Newton and Chandra in 1999 (Branduardi-Raymont et al., 2004; Elsner et al., 2005). New in situ measurements by Juno have detected the ion precipitation that leads to these X-ray emissions. Previous modeling required much higher energy ions (Cravens et al., 1995; Houston et al., 2018; Ozak et al., 2010, 2013), which were difficult to explain with given knowledge of Jupiter's magnetosphere. This forced us to rethink the processes producing X-ray emission from ion precipitation. Schultz et al. (2019) determined not every process was being accounted for in the original precipitation modeling, but simultaneous processes (both target and ion) needed to be considered. This led to a completely new series of processes and cross sections that we have now utilized for the updated heavy ion precipitation model described here. The initial ion energy necessary to produce X-rays has been reduced dramatically and is now well within the heavy ion energy range being measured by the Juno spacecraft.

To summarize the findings of our model:

1. New data, accounting for SIM processes, have shifted the charge state distribution of both oxygen and sulfur to lower energies than before. The repercussions being it now require less energy to strip ions to X-ray producing charge states, resulting in precipitation that does not penetrate as deeply into the atmosphere.
2. Direct excitation is now considered as a new X-ray production mechanism, which adds to the total flux and to the spectrum.
3. Because the ions are not precipitating as deep into the atmosphere as previous models suggested, there is less absorption of photon emission when opacity effects are considered.
4. If an atmosphere of fully mixed constituents is used, the X-ray efficiency is reduced; but emission from ions at the energies measured by JEDI is only reduced by about 15–20% compared to the original atmosphere.
5. While the oxygen collisional data have been carefully checked and published, the analogous data for sulfur utilized here in a preliminary form are now in final preparation and checking for publication.

6. X-ray spectra separated into line emission using Gaussian distributions are producible and can be used in coordination with JEDI ion flux measurements and Earth-orbit-based X-ray observations. When comparing the two, opacity effects need to be considered based on the geometry of the Earth and Jupiter at the time.
7. Approximated synthetic X-ray spectra comparisons with XMM-Newton observations have good agreement with oxygen emission; however, lower energy photoemission needs to be explored further to isolate the discrepancy at lower energies, in the sulfur part of the spectrum. This could be by having an increased sulfur flux or by including emission from electron bremsstrahlung. Although the sulfur data are preliminary, we do not expect any changes to the data to be significant enough to resolve the differences seen.
8. JEDI flux measurements input into the model generate enough X-rays to account for the total X-ray power that has been observed in the past.

This paper has shown that the observed soft X-ray auroral emission from Jupiter can indeed be explained by the precipitation of energy heavy ions (as observed by Juno). Hence, X-ray observation can be used to estimate heavy ion fluxes with energies in excess of ~200 keV/u (i.e., 3 MeV and higher) and to determine the morphology of this precipitation made over the polar caps. Such precipitation has been shown to be associated with downward field-aligned currents, both due to the primary ion precipitation and the resultant secondary electron escape from the atmosphere (Cravens et al., 2003; Houston et al., 2018; Ozak et al., 2010; Ozak et al., 2013). The ion precipitation is also responsible as a source of ionization in the thermosphere, which was explored further in the earlier model presented by Houston et al. (2018). The model established here has very similar atmospheric ion production rates as previously reported. But a deeper discussion is reserved for a future publication, to examine the effects on ionospheric conductivities, which are important for understanding magnetosphere-ionosphere coupling. Much work remains to be done on the Jovian polar aurora.

Appendix A: Additional Oxygen Tables

Here we provide various comprehensive data sets relating to oxygen. Tables A1 and A1 contain all of the altitude integrated ion production from charge exchange and direct excitation collisions. These are followed by Tables A3 through A6 that present the X-ray efficiencies for the relevant oxygen charge states for a wide range of initial ion.

Table A1
Altitude Integrated Ion Production (cm^{-2} s^{-1}) From Charge Exchange Collisions (i.e., TI, SC, and SC+SS) for Oxygen With Incident Ion Energies Between 10 and 25,000 keV/u With No Opacity Effects Considered

	Energy					
Ion charge state	10 keV/u	50 keV/u	75 keV/u	100 keV/u	200 keV/u	300 keV/u
O	2.27E+02	7.67E+02	8.12E+02	8.21E+02	8.26E+02	8.24E+02
O^{+}	1.34E+02	9.43E+02	1.16E+03	1.24E+03	1.28E+03	1.27E+03
O^{++}	1.25E+01	2.24E+02	3.99E+02	5.54E+02	7.11E+02	7.12E+02
O^{3+}	3.57E−01	2.73E+01	8.23E+01	1.78E+02	4.79E+02	5.03E+02
O^{4+}	3.06E−03	1.28E+00	7.01E+00	2.65E+01	2.67E+02	3.66E+02
O^{5+}	—	4.16E−02	4.18E−01	2.90E+00	1.55E+02	4.79E+02
O^{6+}	—	—	1.04E−04	2.08E−03	1.33E+00	1.79E+01
O^{7+}	—	—	—	1.04E−04	9.14E−02	2.33E+00
	500 keV/u	1,000 keV/u	2,000 keV/u	5,000 keV/u	10,000 keV/u	25,000 keV/u
O	8.24E+02	8.23E+02	8.22E+02	8.22E+02	8.21E+02	8.28E+02
O^{+}	1.27E+03	1.27E+03	1.27E+03	1.27E+03	1.27E+03	1.28E+03
O^{++}	1.25E+01	2.24E+02	3.99E+02	5.54E+02	7.11E+02	7.12E+02
O^{3+}	5.03E+02	5.02E+02	5.03E+02	5.02E+02	5.01E+02	5.05E+02
O^{4+}	3.75E+02	3.74E+02	3.74E+02	3.74E+02	3.73E+02	3.77E+02
O^{5+}	6.73E+02	7.00E+02	7.00E+02	6.99E+02	6.98E+02	7.04E+02
O^{6+}	7.01E+01	1.17E+02	1.19E+02	1.19E+02	1.18E+02	1.19E+02
O^{7+}	2.35E+01	1.10E+02	1.49E+02	1.61E+02	1.63E+02	1.64E+02

Note. Everything has been normalized to a single incident ion/cm^{2}/s

Table A2
Altitude Integrated Ion Production ($cm^{-2}\ s^{-1}$) From Direct Excitation Collisions (i.e., SI+SPEX, DI+SPEX, and TEX+SPEX) for Oxygen With Incident Ion Energies Between 10 and 25,000 keV/u With No Opacity Effects Considered

	Energy					
Ion charge state	10 keV/u	50 keV/u	75 keV/u	100 keV/u	200 keV/u	300 keV/u
O	2.53E+02	1.02E+03	1.13E+03	1.17E+03	1.18E+03	1.18E+03
O^{+}	1.94E+01	3.48E+02	5.33E+02	6.30E+02	6.86E+02	6.86E+02
O^{++}	3.21E+00	8.89E+01	1.95E+02	3.23E+02	5.17E+02	5.21E+02
O^{3+}	7.55E−02	7.28E+00	2.91E+01	8.40E+01	3.72E+02	4.10E+02
O^{4+}	7.14E−04	3.04E−01	1.67E+00	8.88E+00	1.43E+02	2.25E+02
O^{5+}	—	5.31E−03	9.45E−02	1.04E+00	1.15E+02	4.43E+02
O^{6+}	—	—	1.04E−04	2.29E−03	1.63E+00	1.97E+01
O^{7+}	—	—	—	—	1.59E−02	9.38E−01
	500 keV/u	1,000 keV/u	2,000 keV/u	5,000 keV/u	10,000 keV/u	25,000 keV/u
O	1.18E+03	1.18E+03	1.18E+03	1.18E+03	1.17E+03	1.18E+03
O^{+}	6.85E+02	6.84E+02	6.83E+02	6.85E+02	6.83E+02	6.89E+02
O^{++}	5.21E+02	5.20E+02	5.20E+02	5.20E+02	5.19E+02	5.23E+02
O^{3+}	4.11E+02	4.10E+02	4.10E+02	4.10E+02	4.09E+02	4.13E+02
O^{4+}	2.39E+02	2.38E+02	2.38E+02	2.38E+02	2.38E+02	2.40E+02
O^{5+}	6.60E+02	6.91E+02	6.91E+02	6.90E+02	6.89E+02	6.96E+02
O^{6+}	7.00E+01	1.09E+02	1.11E+02	1.11E+02	1.11E+02	1.12E+02
O^{7+}	1.47E+01	9.39E+01	1.34E+02	1.48E+02	1.49E+02	1.51E+02

Note. Everything has been normalized to a single incident ion/cm^2/s.

Table A3
The X-Ray Efficiency ($[cm^2 sec]^{-1}[keV/u]^{-1}$) of Outgoing Photons as a Function of Initial Ion Energy Including Opacity Effects

	Atmosphere 1 (Original atmosphere)							
Energy	No opacity		0°		80°		90°	
(keV/u)	O^{6+}	O^{7+}	O^{6+}	O^{7+}	O^{6+}	O^{7+}	O^{6+}	O^{7+}
100	0.00002	—	0.00002	—	0.00002	—	0.00002	—
121	0.00013	—	0.00013	—	0.00013	—	0.00013	—
125	0.00017	0.00001	0.00017	0.00001	0.00017	0.00001	0.00017	0.00001
150	0.00084	0.00004	0.00084	0.00004	0.00084	0.00004	0.00083	0.00004
175	0.00281	0.00017	0.00280	0.00017	0.00280	0.00017	0.00279	0.00017
200	0.00676	0.00045	0.00676	0.00045	0.00675	0.00045	0.00670	0.00045
218	0.01122	0.00083	0.01121	0.00083	0.01120	0.00083	0.01110	0.00082
250	0.02283	0.00201	0.02282	0.00201	0.02278	0.00201	0.02251	0.00199
300	0.04796	0.00569	0.04793	0.00569	0.04780	0.00567	0.04690	0.00560
350	0.07630	0.01209	0.07623	0.01208	0.07591	0.01204	0.07364	0.01182
400	0.10308	0.02163	0.10294	0.02161	0.10232	0.02151	0.09755	0.02098
450	0.12439	0.03339	0.12417	0.03335	0.12311	0.03316	0.11448	0.03205
456	0.12697	0.03509	0.12673	0.03504	0.12560	0.03483	0.11634	0.03363
500	0.13987	0.04676	0.13952	0.04668	0.13787	0.04634	0.12372	0.04429
600	0.15391	0.07349	0.15318	0.07328	0.14981	0.07241	0.11957	0.06671
700	0.15051	0.09296	0.14925	0.09254	0.14353	0.09083	0.09536	0.07866
800	0.14038	0.10470	0.13850	0.10395	0.13006	0.10107	0.06782	0.07982
900	0.12843	0.10958	0.12589	0.10844	0.11476	0.10415	0.04539	0.07304
1,000	0.11703	0.11002	0.11385	0.10843	0.10024	0.10258	0.03000	0.06267
1,250	0.09460	0.10269	0.08997	0.09985	0.07150	0.09008	0.01143	0.03800
1,500	0.07939	0.09270	0.07349	0.08865	0.05176	0.07529	0.00491	0.02157
1,750	0.06784	0.08262	0.06095	0.07756	0.03774	0.06155	0.00251	0.01233
2,000	0.05952	0.07455	0.05169	0.06854	0.02774	0.05030	0.00138	0.00715
5,000	0.02374	0.03229	0.01087	0.02029	0.00113	0.00440	0.00004	0.00018
10,000	0.01182	0.01628	0.00121	0.00373	0.00007	0.00026	—	0.00001
25,000	0.00477	0.00657	0.00003	0.00009	—	0.00001	—	—

Note. No opacity effects and the viewing angles of 0°, 80°, and 90° are displayed for Atmosphere 1. The efficiency shown here is that solely from charge exchange collisions for oxygen. We also include the X-ray efficiencies that correspond to the JEDI energy bins at the time of writing.

Table A4
The X-Ray Efficiency ($[cm^2 sec]^{-1}[keV/u]^{-1}$) of Outgoing Photons as a Function of Initial Ion Energy Including Opacity Effects

Atmosphere 2 (Well-mixed atmosphere)								
Energy	No opacity		0°		80°		90°	
(keV/u)	O^{6+}	O^{7+}	O^{6+}	O^{7+}	O^{6+}	O^{7+}	O^{6+}	O^{7+}
100	0.00002	—	0.00002	—	0.00002	—	0.00002	—
121	0.00013	—	0.00013	—	0.00013	—	0.00013	—
125	0.00017	0.00001	0.00017	0.00001	0.00017	0.00001	0.00017	0.00001
150	0.00084	0.00004	0.00084	0.00004	0.00083	0.00004	0.00081	0.00004
175	0.00281	0.00017	0.00280	0.00017	0.00279	0.00017	0.00270	0.00017
200	0.00676	0.00045	0.00675	0.00045	0.00670	0.00045	0.00646	0.00044
218	0.01122	0.00083	0.01120	0.00083	0.01112	0.00082	0.01065	0.00080
250	0.02283	0.00201	0.02278	0.00201	0.02257	0.00200	0.02135	0.00193
300	0.04796	0.00569	0.04783	0.00568	0.04719	0.00563	0.04346	0.00536
350	0.07630	0.01209	0.07601	0.01206	0.07462	0.01192	0.06620	0.01119
400	0.10308	0.02163	0.10255	0.02156	0.10008	0.02125	0.08452	0.01957
450	0.12439	0.03339	0.12357	0.03326	0.11976	0.03267	0.09518	0.02940
456	0.12697	0.03509	0.12610	0.03494	0.12210	0.03431	0.09618	0.03079
500	0.13987	0.04676	0.13871	0.04653	0.13337	0.04554	0.09835	0.03988
600	0.15391	0.07349	0.15199	0.07296	0.14328	0.07076	0.08631	0.05738
700	0.15051	0.09296	0.14783	0.09204	0.13597	0.08829	0.06296	0.06434
800	0.14038	0.10470	0.13701	0.10330	0.12234	0.09779	0.04145	0.06216
900	0.12843	0.10958	0.12444	0.10768	0.10746	0.10042	0.02621	0.05453
1,000	0.11703	0.11002	0.11248	0.10761	0.09361	0.09867	0.01673	0.04529
1,250	0.09460	0.10269	0.08885	0.09904	0.06658	0.08638	0.00626	0.02641
1,500	0.07939	0.09270	0.07256	0.08792	0.04817	0.07213	0.00270	0.01487
1,750	0.06784	0.08262	0.06018	0.07692	0.03512	0.05895	0.00140	0.00850
2,000	0.05952	0.07455	0.05103	0.06798	0.02581	0.04817	0.00077	0.00493
5,000	0.02374	0.03229	0.01072	0.02013	0.00105	0.00423	0.00003	0.00012
10,000	0.01182	0.01628	0.00119	0.00369	0.00007	0.00025	—	0.00001
25,000	0.00477	0.00657	0.00003	0.00009	—	0.00001	—	—

Note. No opacity effects and the viewing angles of 0°, 80°, and 90° are displayed for Atmosphere 2. The efficiency shown here is that solely from charge exchange collisions for oxygen. We also include the X-ray efficiencies that correspond to the JEDI energy bins at the time of writing.

Table A5
The X-Ray Efficiency ($[cm^2 sec]^{-1}[keV/u]^{-1}$) of Outgoing Photons as a Function of Initial Ion Energy Including Opacity Effects

Atmosphere 1 (Original atmosphere)								
Energy	No opacity		0°		80°		90°	
(keV/u)	O^{6+}	O^{7+}	O^{6+}	O^{7+}	O^{6+}	O^{7+}	O^{6+}	O^{7+}
100	0.00003	—	0.00003	—	0.00003	—	0.00003	—
121	0.00014	—	0.00014	—	0.00014	—		
125	0.00020	—	0.00020	—	0.00020	—	0.00020	—
150	0.00098	—	0.00098	—	0.00098	—	0.00097	—
175	0.00313	0.00002	0.00313	0.00002	0.00313	0.00002	0.00311	0.00002
200	0.00747	0.00007	0.00746	0.00007	0.00745	0.00007	0.00740	0.00007
218	0.01242	0.00017	0.01242	0.00017	0.01240	0.00017	0.01230	0.00017
250	0.02443	0.00054	0.02442	0.00054	0.02437	0.00054	0.02408	0.00054
300	0.04852	0.00194	0.04849	0.00194	0.04835	0.00193	0.04741	0.00192
350	0.07465	0.00498	0.07458	0.00498	0.07426	0.00497	0.07195	0.00492
400	0.09801	0.01013	0.09788	0.01012	0.09726	0.01010	0.09252	0.00994
450	0.11545	0.01736	0.11523	0.01735	0.11421	0.01729	0.10580	0.01690
456	0.11761	0.01849	0.11738	0.01848	0.11629	0.01842	0.10727	0.01798
500	0.12752	0.02654	0.12719	0.02652	0.12562	0.02641	0.11202	0.02556
600	0.13589	0.04735	0.13522	0.04728	0.13209	0.04696	0.10395	0.04400
700	0.13063	0.06541	0.12949	0.06525	0.12430	0.06448	0.08060	0.05705
800	0.12044	0.07738	0.11876	0.07706	0.11125	0.07557	0.05622	0.06109
900	0.10968	0.08317	0.10744	0.08263	0.09765	0.08012	0.03734	0.05722
1,000	0.09991	0.08502	0.09713	0.08419	0.08527	0.08044	0.02481	0.04944
1,250	0.08049	0.08112	0.07653	0.07945	0.06070	0.07217	0.00968	0.02952
1,500	0.06746	0.07423	0.06245	0.07164	0.04397	0.06090	0.00434	0.01657
1,750	0.05762	0.06658	0.05179	0.06316	0.03211	0.04975	0.00233	0.00939
2,000	0.05053	0.06048	0.04391	0.05623	0.02363	0.04057	0.00138	0.00550
5,000	0.02016	0.02673	0.00932	0.01641	0.00104	0.00311	0.00015	0.00025
10,000	0.01006	0.01347	0.00107	0.00266	0.00012	0.00022	0.00006	0.00007
25,000	0.00406	0.00544	0.00005	0.00009	0.00003	0.00003	0.00003	0.00003

Note. No opacity effects and the viewing angles of 0°, 80°, and 90° are displayed for Atmosphere 1. The efficiency shown here is that solely from direct excitation collisions for oxygen.

Table A6
The X-Ray Efficiency $([cm^2 sec]^{-1}[keV/u]^{-1})$ *of Outgoing Photons as a Function of Initial Ion Energy Including Opacity Effects*

	Atmosphere 2 (Well-mixed atmosphere)							
Energy	No opacity		0°		80°		90°	
(keV/u)	O^{6+}	O^{7+}	O^{6+}	O^{7+}	O^{6+}	O^{7+}	O^{6+}	O^{7+}
100	0.00003	—	0.00003	—	0.00003	—	0.00003	—
121	0.00014	—	0.00014	—	0.00014	—	0.00013	—
125	0.00020	—	0.00020	—	0.00020	—	0.00019	—
150	0.00098	—	0.00098	—	0.00097	—	0.00095	—
175	0.00313	0.00002	0.00313	0.00002	0.00311	0.00002	0.00302	0.00002
200	0.00747	0.00007	0.00745	0.00007	0.00741	0.00007	0.00714	0.00007
218	0.01242	0.00017	0.01240	0.00017	0.01231	0.00017	0.01179	0.00017
250	0.02443	0.00054	0.02438	0.00054	0.02414	0.00054	0.02280	0.00053
300	0.04852	0.00194	0.04838	0.00193	0.04772	0.00192	0.04382	0.00185
350	0.07465	0.00498	0.07435	0.00497	0.07297	0.00493	0.06447	0.00469
400	0.09801	0.01013	0.09749	0.01010	0.09508	0.01000	0.07979	0.00933
450	0.11545	0.01736	0.11466	0.01731	0.11103	0.01708	0.08743	0.01561
456	0.11761	0.01849	0.11678	0.01844	0.11297	0.01819	0.08812	0.01656
500	0.12752	0.02654	0.12643	0.02645	0.12143	0.02603	0.08837	0.02315
600	0.13589	0.04735	0.13414	0.04711	0.12623	0.04602	0.07426	0.03805
700	0.13063	0.06541	0.12825	0.06495	0.11769	0.06282	0.05266	0.04678
800	0.12044	0.07738	0.11749	0.07664	0.10464	0.07322	0.03415	0.04740
900	0.10968	0.08317	0.10621	0.08210	0.09147	0.07727	0.02157	0.04220
1,000	0.09991	0.08502	0.09598	0.08361	0.07968	0.07730	0.01396	0.03501
1,250	0.08049	0.08112	0.07559	0.07883	0.05658	0.06902	0.00546	0.01989
1,500	0.06746	0.07423	0.06167	0.07105	0.04095	0.05812	0.00254	0.01105
1,750	0.05762	0.06658	0.05114	0.06264	0.02990	0.04744	0.00142	0.00628
2,000	0.05053	0.06048	0.04336	0.05576	0.02200	0.03866	0.00088	0.00369
5,000	0.02016	0.02673	0.00919	0.01626	0.00098	0.00297	0.00013	0.00021
10,000	0.01006	0.01347	0.00106	0.00264	0.00012	0.00022	0.00006	0.00006
25,000	0.00406	0.00544	0.00005	0.00008	0.00003	0.00003	0.00003	0.00003

Note. No opacity effects and the viewing angles of 0°, 80°, and 90° are displayed for Atmosphere 2. The efficiency shown here is that solely from direct excitation collisions for oxygen.

Appendix B: Additional Sulfur Tables

Here we provide various comprehensive data sets relating to sulfur. Tables B1 and B2 contain all of the altitude integrated ion production from charge exchange and direct excitation collisions. These are followed by Tables B3 through B10 that present the X-ray efficiencies for the relevant sulfur charge states for a wide range of initial ion energies.

Table B1

Altitude Integrated Ion Production (cm^{-2} s^{-1}) From Charge Exchange Collisions (i.e., TI, SC, and SC+SS) for Sulfur With Incident Ion Energies Between 10 and 2,000 keV/u With No Opacity Effects Considered

	Energy								
Ion charge state	10 keV/u	50 keV/u	75 keV/u	100 keV/u	200 keV/u	300 keV/u	500 keV/u	1,000 keV/u	2,000 keV/u
S	2.33E+02	9.94E+02	1.07E+03	1.08E+03	1.08E+03	1.08E+03	1.08E+03	1.08E+03	1.08E+03
S^{+}	2.07E+02	2.24E+03	2.66E+03	2.78E+03	2.81E+03	2.81E+03	2.81E+03	2.81E+03	2.81E+03
S^{++}	3.88E+01	9.92E+02	1.51E+03	1.85E+03	2.09E+03	2.09E+03	2.09E+03	2.09E+03	2.09E+03
S^{3+}	2.16E+00	1.79E+02	4.61E+02	8.23E+02	1.42E+03	1.45E+03	1.45E+03	1.45E+03	1.45E+03
S^{4+}	3.01E−02	1.39E+01	6.23E+01	1.79E+02	8.22E+02	9.50E+02	9.56E+02	9.56E+02	9.56E+02
S^{5+}	3.57E−04	7.27E−01	5.21E+00	2.77E+01	6.14E+02	1.18E+03	1.33E+03	1.33E+03	1.33E+03
S^{6+}	—	1.89E−03	3.04E−02	3.29E−01	4.12E+01	1.87E+02	3.28E+02	3.29E+02	3.30E+02
S^{7+}	—	1.02E−04	6.12E−04	1.00E−02	4.99E+00	5.56E+01	1.86E+02	1.92E+02	1.92E+02
S^{8+}	—	—	—	1.53E−04	3.35E−01	1.03E+01	9.98E+01	1.16E+02	1.16E+02
S^{9+}	—	—	—	—	2.23E−02	1.87E+00	6.18E+01	8.92E+01	8.92E+01
S^{10+}	—	—	—	—	7.14E−04	2.31E−01	2.60E+01	5.34E+01	5.34E+01
S^{11+}	—	—	—	—	5.10E−05	3.42E−02	1.66E+01	6.12E+01	6.13E+01
S^{12+}	—	—	—	—	—	7.96E−03	1.11E+01	7.91E+01	8.15E+01
S^{13+}	—	—	—	—	—	1.12E−03	1.03E+01	2.27E+02	2.78E+02
S^{14+}	—	—	—	—	—	—	7.41E−02	1.19E+01	3.81E+01
S^{15+}	—	—	—	—	—	—	4.14E−02	6.96E+00	2.39E+01

Note. Everything has been normalized to a single incident ion/cm^2/s.

Table B2
Altitude Integrated Ion Production (cm^{-2} s^{-1}) From Direct Excitation Collisions (i.e., SI+SPEX, DI+SPEX, and TEX+SPEX) for Sulfur With Incident Ion Energies Between 10 and 2,000 keV/u With No Opacity Effects Considered

	Energy				
Ion charge state	10 keV/u	50 keV/u	75 keV/u	100 keV/u	200 keV/u
S	3.33E+02	2.58E+03	2.95E+03	3.05E+03	3.08E+03
S^{+}	4.71E+01	1.22E+03	1.72E+03	1.98E+03	2.12E+03
S^{++}	2.07E+00	1.78E+02	4.77E+02	7.89E+02	1.15E+03
S^{3+}	1.57E−01	3.13E+01	1.50E+02	3.73E+02	1.01E+03
S^{4+}	2.26E−03	2.27E+00	1.34E+01	6.17E+01	7.08E+02
S^{5+}	—	1.07E−01	1.52E+00	1.20E+01	5.16E+02
S^{6+}	—	1.51E−04	3.92E−03	7.59E−02	1.50E+01
S^{7+}	—	—	—	6.53E-−04	9.02E−01
S^{8+}	—	—	—	—	1.16E−01
S^{9+}	—	—	—	—	4.12E−03
S^{10+}	—	—	—	—	5.02E−04
S^{11+}	—	—	—	—	5.02E-05
S^{12+}	—	—	—	—	—
S^{13+}	—	—	—	—	—
S^{14+}	—	—	—	—	—
S^{15+}	—	—	—	—	—
	300 keV/u	500 keV/u	1,000 keV/u	2,000 keV/u	
S	3.08E+03	3.07E+03	3.08E+03	3.08E+03	
S^{+}	2.12E+03	2.12E+03	2.12E+03	2.12E+03	
S^{++}	1.16E+03	1.16E+03	1.16E+03	1.16E+03	
S^{3+}	1.08E+03	1.08E+03	1.08E+03	1.08E+03	
S^{4+}	9.24E+02	9.41E+02	9.41E+02	9.42E+02	
S^{5+}	1.20E+03	1.42E+03	1.42E+03	1.42E+03	
S^{6+}	9.54E+01	2.01E+02	2.03E+02	2.03E+02	
S^{7+}	1.72E+01	9.47E+01	1.00E+02	1.00E+02	
S^{8+}	5.32E+00	6.71E+01	7.97E+01	7.96E+01	
S^{9+}	6.79E−01	3.37E+01	5.15E+01	5.15E+01	
S^{10+}	8.24E−02	1.65E+01	3.83E+01	3.80E+01	
S^{11+}	1.30E−02	9.15E+00	3.52E+01	3.54E+01	
S^{12+}	2.15E−03	6.59E+00	5.89E+01	6.06E+01	
S^{13+}	6.50E−04	1.15E+01	2.46E+02	3.00E+02	
S^{14+}	—	1.25E−01	1.05E+01	2.97E+01	
S^{15+}	—	7.21E−02	2.08E+02	2.88E+03	

Note. Everything has been normalized to a single incident ion/cm^{2}/s.

Table B3

The X-Ray Efficiency ($[cm^2 sec]^{-1}[keV/u]^{-1}$) of Outgoing Photons as a Function of initial Ion Energy Including Opacity Effects

	Atmosphere 1 (Original atmosphere)						
Energy (keV/u)	No opacity						
	S^{8+}	S^{9+}	S^{10+}	S^{11+}	S^{12+}	S^{13+}	S^{14+}
125	0.00002	—	—	—	—	—	—
150	0.00010	—	—	—	—	—	—
175	0.00048	0.00002	—	—	—	—	—
200	0.00168	0.00011	—	—	—	—	—
250	0.01033	0.00119	0.00009	0.00001	—	—	—
300	0.03435	0.00622	0.00077	0.00011	0.00003	—	—
350	0.07751	0.02099	0.00377	0.00086	0.00026	0.00007	—
400	0.13211	0.05073	0.01291	0.00427	0.00181	0.00076	—
450	0.17796	0.09057	0.03048	0.01437	0.00774	0.00495	0.00002
500	0.19957	0.12365	0.05208	0.03326	0.02226	0.02065	0.00015
600	0.19061	0.14001	0.07467	0.06741	0.06023	0.08874	0.00122
700	0.16565	0.12694	0.07368	0.07715	0.08247	0.15869	0.00334
800	0.14505	0.11168	0.06641	0.07405	0.08766	0.20345	0.00609
900	0.12878	0.09920	0.05931	0.06757	0.08488	0.22342	0.00907
1,000	0.11593	0.08921	0.05339	0.06117	0.07910	0.22688	0.01191
1,250	0.09275	0.07149	0.04272	0.04902	0.06474	0.20672	0.01681
1,500	0.07726	0.05951	0.03565	0.04084	0.05431	0.18070	0.01895
1,750	0.06618	0.05094	0.03055	0.03507	0.04660	0.15759	0.01950
2,000	0.05796	0.04462	0.02672	0.03063	0.04077	0.13882	0.01907
	0°						
	S^{8+}	S^{9+}	S^{10+}	S^{11+}	S^{12+}	S^{13+}	S^{14+}
125	0.00002	—	—	—	—	—	—
150	0.00010	—	—	—	—	—	—
175	0.00047	0.00002	—	—	—	—	—
200	0.00167	0.00011	—	—	—	—	—
250	0.01024	0.00119	0.00009	0.00001	—	—	—
300	0.03391	0.00619	0.00077	0.00011	0.00003	—	—
350	0.07618	0.02083	0.00375	0.00086	0.00026	0.00007	—
400	0.12911	0.05025	0.01284	0.00426	0.00181	0.00075	—
450	0.17269	0.08948	0.03027	0.01433	0.00773	0.00494	0.00002
500	0.19194	0.12176	0.05162	0.03314	0.02221	0.02061	0.00015
600	0.17921	0.13648	0.07358	0.06701	0.05998	0.08846	0.00121
700	0.15150	0.12194	0.07190	0.07635	0.08191	0.15785	0.00334
800	0.12849	0.10528	0.06388	0.07278	0.08666	0.20172	0.00607
900	0.11009	0.09141	0.05598	0.06572	0.08331	0.22044	0.00904
1,000	0.09534	0.08011	0.04923	0.05867	0.07686	0.22232	0.01185
1,250	0.06888	0.05982	0.03679	0.04496	0.06068	0.19741	0.01664
1,500	0.05167	0.04624	0.02854	0.03564	0.04878	0.16689	0.01860
1,750	0.03981	0.03672	0.02272	0.02910	0.04003	0.14030	0.01896
2,000	0.03125	0.02976	0.01839	0.02411	0.03343	0.11879	0.01834

Note. No opacity effects and the viewing angle of 0° are displayed for Atmosphere 1. The efficiency shown here is that solely from charge exchange collisions for sulfur.

Table B4
The X-Ray Efficiency ($[cm^2 sec]^{-1}[keV/u]^{-1}$) of Outgoing Photons as a Function of Initial Ion Energy Including Opacity Effects

Atmosphere 1 (Original atmosphere)							
Energy (keV/u)	80°						
	S^{8+}	S^{9+}	S^{10+}	S^{11+}	S^{12+}	S^{13+}	S^{14+}
125	0.00002	—	—	—	—	—	—
150	0.00010	—	—	—	—	—	—
175	0.00046	0.00002	—	—	—	—	—
200	0.00162	0.00011	—	—	—	—	—
250	0.00984	0.00116	0.00009	0.00001	—	—	—
300	0.03200	0.00603	0.00076	0.00011	0.00003	—	—
350	0.07051	0.02013	0.00367	0.00085	0.00026	0.00007	—
400	0.11672	0.04811	0.01250	0.00421	0.00179	0.00075	—
450	0.15163	0.08471	0.02930	0.01413	0.00765	0.00490	0.00002
500	0.16248	0.11359	0.04957	0.03258	0.02194	0.02041	0.00015
600	0.13816	0.12174	0.06880	0.06515	0.05884	0.08713	0.00121
700	0.10425	0.10197	0.06436	0.07277	0.07931	0.15406	0.00331
800	0.07775	0.08107	0.05370	0.06721	0.08217	0.19411	0.00601
900	0.05797	0.06380	0.04334	0.05798	0.07651	0.20778	0.00890
1,000	0.04345	0.05016	0.03452	0.04872	0.06752	0.20369	0.01161
1,250	0.02220	0.02817	0.01954	0.03095	0.04572	0.16341	0.01597
1,500	0.01231	0.01657	0.01152	0.02018	0.03088	0.12204	0.01739
1,750	0.00735	0.01025	0.00715	0.01371	0.02135	0.09018	0.01724
2,000	0.00466	0.00662	0.00459	0.00952	0.01510	0.06700	0.01618
	90°						
	S^{8+}	S^{9+}	S^{10+}	S^{11+}	S^{12+}	S^{13+}	S^{14+}
125	0.00001	—	—	—	—	—	—
150	0.00009	—	—	—	—	—	—
175	0.00041	0.00002	—	—	—	—	—
200	0.00140	0.00010	—	—	—	—	—
250	0.00796	0.00105	0.00008	0.00001	—	—	—
300	0.02387	0.00519	0.00068	0.00011	0.00003	—	—
350	0.04837	0.01656	0.00324	0.00080	0.00025	0.00006	—
400	0.07273	0.03760	0.01071	0.00391	0.00170	0.00072	—
450	0.08421	0.06225	0.02418	0.01292	0.00718	0.00468	0.00002
500	0.07789	0.07701	0.03900	0.02926	0.02035	0.01935	0.00015
600	0.04480	0.06372	0.04579	0.05407	0.05178	0.07970	0.00118
700	0.02137	0.03639	0.03238	0.05213	0.06319	0.13267	0.00318
800	0.01059	0.01843	0.01833	0.03799	0.05554	0.15203	0.00566
900	0.00599	0.00957	0.00963	0.02374	0.04068	0.14184	0.00817
1,000	0.00379	0.00562	0.00534	0.01387	0.02666	0.11634	0.01033
1,250	0.00163	0.00220	0.00186	0.00432	0.00872	0.05583	0.01299
1,500	0.00088	0.00113	0.00092	0.00196	0.00368	0.02668	0.01312
1,750	0.00053	0.00066	0.00053	0.00110	0.00192	0.01381	0.01241
2,000	0.00035	0.00043	0.00034	0.00068	0.00114	0.00763	0.01131

Note. Viewing angles of 80° and 90° are displayed for Atmosphere 1. The efficiency shown here is that solely from charge exchange collisions for sulfur.

Table B5
The X-Ray Efficiency ($[cm^2 sec]^{-1}[keV/u]^{-1}$) of Outgoing Photons as a Function of Initial Ion Energy Including Opacity Effects

	Atmosphere 2 (Well-mixed atmosphere)						
Energy	No opacity						
(keV/u)	S^{8+}	S^{9+}	S^{10+}	S^{11+}	S^{12+}	S^{13+}	S^{14+}
125	0.00002	—	—	—	—	—	—
150	0.00010	—	—	—	—	—	—
175	0.00048	0.00002	—	—	—	—	—
200	0.00168	0.00011	—	—	—	—	—
250	0.01033	0.00119	0.00009	0.00001	—	—	—
300	0.03435	0.00622	0.00077	0.00011	0.00003	—	—
350	0.07751	0.02099	0.00377	0.00086	0.00026	0.00007	—
400	0.13211	0.05073	0.01291	0.00427	0.00181	0.00076	—
450	0.17796	0.09057	0.03048	0.01437	0.00774	0.00495	0.00002
500	0.19957	0.12365	0.05208	0.03326	0.02226	0.02065	0.00015
600	0.19061	0.14001	0.07467	0.06741	0.06023	0.08874	0.00122
700	0.16565	0.12694	0.07368	0.07715	0.08247	0.15869	0.00334
800	0.14505	0.11168	0.06641	0.07405	0.08766	0.20345	0.00609
900	0.12878	0.09920	0.05931	0.06757	0.08488	0.22342	0.00907
1,000	0.11593	0.08921	0.05339	0.06117	0.07910	0.22688	0.01191
1,250	0.09275	0.07149	0.04272	0.04902	0.06474	0.20672	0.01681
1,500	0.07726	0.05951	0.03565	0.04084	0.05431	0.18070	0.01895
1,750	0.06618	0.05094	0.03055	0.03507	0.04660	0.15759	0.01950
2,000	0.05796	0.04462	0.02672	0.03063	0.04077	0.13882	0.01907
	0°						
	S^{8+}	S^{9+}	S^{10+}	S^{11+}	S^{12+}	S^{13+}	S^{14+}
125	0.00002	—	—	—	—	—	—
150	0.00010	—	—	—	—	—	—
175	0.00047	0.00002	—	—	—	—	—
200	0.00165	0.00011	—	—	—	—	—
250	0.01012	0.00118	0.00009	0.00001	—	—	—
300	0.03339	0.00613	0.00076	0.00011	0.00003	—	—
350	0.07476	0.02060	0.00371	0.00086	0.00026	0.00007	—
400	0.12624	0.04958	0.01268	0.00422	0.00180	0.00075	—
450	0.16819	0.08807	0.02984	0.01421	0.00768	0.00492	0.00002
500	0.18611	0.11951	0.05076	0.03283	0.02204	0.02050	0.00015
600	0.17222	0.13299	0.07182	0.06607	0.05935	0.08780	0.00121
700	0.14454	0.11795	0.06954	0.07481	0.08066	0.15619	0.00333
800	0.12201	0.10123	0.06124	0.07081	0.08486	0.19885	0.00604
900	0.10425	0.08755	0.05331	0.06354	0.08112	0.21643	0.00899
1,000	0.09015	0.07658	0.04670	0.05649	0.07450	0.21748	0.01177
1,250	0.06503	0.05707	0.03477	0.04311	0.05850	0.19203	0.01650
1,500	0.04875	0.04409	0.02694	0.03414	0.04696	0.16200	0.01842
1,750	0.03754	0.03500	0.02144	0.02786	0.03851	0.13607	0.01877
2,000	0.02947	0.02836	0.01735	0.02308	0.03216	0.11517	0.01814

Note. No opacity effects and the viewing angle of 0° are displayed for Atmosphere 2. The efficiency shown here is that solely from charge exchange collisions for sulfur.

Table B6
The X-Ray Efficiency ($[cm^2 sec]^{-1}[keV/u]^{-1}$) of Outgoing Photons as a Function of Initial Ion Energy Including Opacity Effects

Atmosphere 2 (Well-mixed atmosphere)

Energy	80°						
(keV/u)	S^{8+}	S^{9+}	S^{10+}	S^{11+}	S^{12+}	S^{13+}	S^{14+}
125	0.00002	—	—	—	—	—	—
150	0.00009	—	—	—	—	—	—
175	0.00044	0.00002	—	—	—	—	—
200	0.00154	0.00011	—	—	—	—	—
250	0.00922	0.00112	0.00008	0.00001	—	—	—
300	0.02947	0.00572	0.00072	0.00011	0.00003	—	—
350	0.06386	0.01891	0.00347	0.00082	0.00025	0.00007	—
400	0.10384	0.04470	0.01169	0.00404	0.00173	0.00073	—
450	0.13230	0.07776	0.02711	0.01348	0.00738	0.00478	0.00002
500	0.13862	0.10275	0.04526	0.03089	0.02106	0.01984	0.00015
600	0.11235	0.10593	0.06038	0.06028	0.05546	0.08362	0.00119
700	0.08137	0.08516	0.05375	0.06509	0.07285	0.14540	0.00325
800	0.05905	0.06551	0.04272	0.05787	0.07320	0.17956	0.00587
900	0.04337	0.05047	0.03323	0.04827	0.06613	0.18824	0.00866
1,000	0.03227	0.03926	0.02591	0.03964	0.05694	0.18111	0.01123
1,250	0.01640	0.02188	0.01442	0.02471	0.03752	0.14143	0.01531
1,500	0.00909	0.01286	0.00847	0.01609	0.02521	0.10477	0.01662
1,750	0.00543	0.00796	0.00526	0.01096	0.01743	0.07731	0.01647
2,000	0.00345	0.00514	0.00338	0.00764	0.01236	0.05754	0.01547
	90°						
	S^{8+}	S^{9+}	S^{10+}	S^{11+}	S^{12+}	S^{13+}	S^{14+}
125	0.00001	—	—	—	—	—	—
150	0.00007	—	—	—	—	—	—
175	0.00034	0.00002	—	—	—	—	—
200	0.00113	0.00009	—	—	—	—	—
250	0.00609	0.00086	0.00007	0.00001	—	—	—
300	0.01732	0.00410	0.00055	0.00009	0.00002	—	—
350	0.03359	0.01259	0.00249	0.00067	0.00022	0.00006	—
400	0.04824	0.02752	0.00793	0.00320	0.00144	0.00064	—
450	0.05301	0.04366	0.01719	0.01029	0.00597	0.00411	0.00002
500	0.04589	0.05121	0.02633	0.02257	0.01652	0.01678	0.00014
600	0.02259	0.03628	0.02626	0.03697	0.03823	0.06468	0.00111
700	0.00948	0.01756	0.01518	0.03026	0.04100	0.09898	0.00293
800	0.00450	0.00803	0.00724	0.01850	0.03111	0.10298	0.00510
900	0.00257	0.00410	0.00349	0.01006	0.01997	0.08746	0.00724
1,000	0.00164	0.00244	0.00194	0.00542	0.01186	0.06631	0.00905
1,250	0.00071	0.00097	0.00070	0.00168	0.00362	0.02883	0.01131
1,500	0.00038	0.00050	0.00035	0.00078	0.00153	0.01334	0.01163
1,750	0.00023	0.00029	0.00020	0.00044	0.00080	0.00680	0.01122
2,000	0.00015	0.00019	0.00013	0.00028	0.00048	0.00373	0.01044

Note. Viewing angles of 80° and 90° are displayed for Atmosphere 2. The efficiency shown here is that solely from charge exchange collisions for sulfur.

Table B7

The X-Ray Efficiency ($[cm^2 sec]^{-1}[keV/u]^{-1}$) of Outgoing Photons as a Function of Initial Ion Energy Including Opacity Effects

Atmosphere 1 (Original atmosphere)							
Energy	No opacity						
(keV/u)	S^{8+}	S^{9+}	S^{10+}	S^{11+}	S^{12+}	S^{13+}	S^{14+}
125	—	—	—	—	—	—	—
150	0.00003	—	—	—	—	—	—
175	0.00013	—	—	—	—	—	—
200	0.00060	0.00002	—	—	—	—	—
250	0.00455	0.00035	0.00003	—	—	—	—
300	0.01774	0.00231	0.00027	0.00004	0.00001	0.00001	—
350	0.04474	0.00900	0.00164	0.00039	0.00010	0.00008	—
400	0.08190	0.02446	0.00655	0.00210	0.00079	0.00081	—
450	0.11585	0.04698	0.01763	0.00764	0.00404	0.00548	—
500	0.13365	0.06738	0.03289	0.01821	0.01317	0.02286	—
600	0.13013	0.07984	0.05156	0.03814	0.04072	0.09703	—
700	0.11346	0.07309	0.05221	0.04407	0.05900	0.17309	—
800	0.09936	0.06444	0.04732	0.04241	0.06448	0.22100	0.00001
900	0.08822	0.05710	0.04235	0.03873	0.06317	0.24218	0.00001
1,000	0.07929	0.05126	0.03798	0.03508	0.05871	0.24513	0.00001
1,250	0.06358	0.04104	0.03041	0.02820	0.04796	0.22260	0.00001
1,500	0.05286	0.03429	0.02530	0.02351	0.04016	0.19461	0.00002
1,750	0.04544	0.02937	0.02172	0.02016	0.03447	0.16986	0.00002
2,000	0.03967	0.02567	0.01898	0.01767	0.03015	0.14960	0.00002
	0°						
	S^{8+}	S^{9+}	S^{10+}	S^{11+}	S^{12+}	S^{13+}	S^{14+}
125	—	—	—	—	—	—	—
150	0.00003	—	—	—	—	—	—
175	0.00013	—	—	—	—	—	—
200	0.00059	0.00002	—	—	—	—	—
250	0.00451	0.00035	0.00003	—	—	—	—
300	0.01753	0.00230	0.00027	0.00004	0.00001	0.00001	—
350	0.04404	0.00894	0.00163	0.00039	0.00010	0.00008	—
400	0.08018	0.02425	0.00651	0.00209	0.00079	0.00081	—
450	0.11267	0.04648	0.01751	0.00761	0.00404	0.00547	—
500	0.12890	0.06645	0.03262	0.01813	0.01314	0.02282	—
600	0.12277	0.07801	0.05083	0.03786	0.04054	0.09677	—
700	0.10418	0.07044	0.05097	0.04351	0.05857	0.17232	—
800	0.08836	0.06100	0.04553	0.04151	0.06369	0.21940	0.00001
900	0.07571	0.05290	0.03995	0.03742	0.06190	0.23937	0.00001
1,000	0.06546	0.04635	0.03495	0.03332	0.05688	0.24074	0.00001
1,250	0.04740	0.03475	0.02604	0.02534	0.04458	0.21312	0.00001
1,500	0.03547	0.02711	0.02007	0.01987	0.03553	0.18011	0.00001
1,750	0.02743	0.02166	0.01593	0.01601	0.02897	0.15135	0.00002
2,000	0.02147	0.01760	0.01283	0.01314	0.02400	0.12789	0.00002

Note. No opacity effects and the viewing angle of 0° are displayed for Atmosphere 1. The efficiency shown here is that solely from direct excitation collisions for sulfur.

Table B8

The X-Ray Efficiency ($[cm^2 sec]^{-1} [keV/u]^{-1}$) of Outgoing Photons as a Function of Initial Ion Energy Including Opacity Effects

	Atmosphere 1 (Original atmosphere)						
Energy (keV/u)	80°						
	S^{8+}	S^{9+}	S^{10+}	S^{11+}	S^{12+}	S^{13+}	S^{14+}
125	—	—	—	—	—	—	—
150	0.00003	—	—	—	—	—	—
175	0.00013	—	—	—	—	—	—
200	0.00058	0.00002	—	—	—	—	—
250	0.00435	0.00034	0.00003	—	—	—	—
300	0.01663	0.00225	0.00027	0.00004	0.00001	0.00001	—
350	0.04099	0.00867	0.00160	0.00039	0.00010	0.00008	—
400	0.07301	0.02332	0.00635	0.00206	0.00079	0.00080	—
450	0.09983	0.04424	0.01696	0.00748	0.00399	0.00544	—
500	0.11030	0.06238	0.03137	0.01776	0.01297	0.02265	—
600	0.09587	0.07025	0.04762	0.03657	0.03972	0.09554	—
700	0.07267	0.05965	0.04568	0.04103	0.05659	0.16875	—
800	0.05414	0.04776	0.03827	0.03764	0.06014	0.21207	0.00001
900	0.04034	0.03773	0.03083	0.03206	0.05643	0.22680	0.00001
1,000	0.03017	0.02981	0.02433	0.02647	0.04928	0.22159	0.00001
1,250	0.01547	0.01713	0.01358	0.01595	0.03228	0.17560	0.00001
1,500	0.00859	0.01035	0.00794	0.00980	0.02095	0.12857	0.00001
1,750	0.00523	0.00655	0.00491	0.00630	0.01393	0.09243	0.00001
2,000	0.00338	0.00430	0.00317	0.00419	0.00944	0.06624	0.00001
	90°						
	S^{8+}	S^{9+}	S^{10+}	S^{11+}	S^{12+}	S^{13+}	S^{14+}
125	—	—	—	—	—	—	—
150	0.00002	—	—	—	—	—	—
175	0.00012	—	—	—	—	—	—
200	0.00050	0.00002	—	—	—	—	—
250	0.00358	0.00031	0.00002	—	—	—	—
300	0.01267	0.00196	0.00024	0.00004	0.00001	0.00001	—
350	0.02877	0.00727	0.00141	0.00036	0.00009	0.00007	—
400	0.04675	0.01867	0.00546	0.00189	0.00074	0.00077	—
450	0.05721	0.03341	0.01411	0.00674	0.00373	0.00521	—
500	0.05483	0.04355	0.02498	0.01562	0.01200	0.02156	—
600	0.03238	0.03846	0.03223	0.02923	0.03473	0.08782	—
700	0.01558	0.02249	0.02341	0.02754	0.04456	0.14553	—
800	0.00787	0.01159	0.01337	0.01911	0.03965	0.16435	0.00001
900	0.00463	0.00614	0.00715	0.01129	0.02864	0.14966	0.00001
1,000	0.00307	0.00371	0.00406	0.00634	0.01796	0.11821	0.00001
1,250	0.00156	0.00164	0.00160	0.00214	0.00546	0.05164	0.00001
1,500	0.00097	0.00097	0.00095	0.00112	0.00240	0.02350	0.00001
1,750	0.00070	0.00067	0.00063	0.00074	0.00137	0.01180	0.00001
2,000	0.00055	0.00050	0.00047	0.00055	0.00088	0.00649	0.00001

Note. Viewing angles of 80° and 90° are displayed for Atmosphere 1. The efficiency shown here is that solely from direct excitation collisions for sulfur.

Table B9
The X-Ray Efficiency ($[cm^2 sec]^{-1} [keV/u]^{-1}$) of Outgoing Photons as a Function of Initial Ion Energy Including Opacity Effects

	Atmosphere 2 (Well-mixed atmosphere)						
Energy	No opacity						
(keV/u)	S^{8+}	S^{9+}	S^{10+}	S^{11+}	S^{12+}	S^{13+}	S^{14+}
125	—	—	—	—	—	—	—
150	0.00003	—	—	—	—	—	—
175	0.00013	—	—	—	—	—	—
200	0.00060	0.00002	—	—	—	—	—
250	0.00455	0.00035	0.00003	—	—	—	—
300	0.01774	0.00231	0.00027	0.00004	0.00001	0.00001	—
350	0.04474	0.00900	0.00164	0.00039	0.00010	0.00008	—
400	0.08190	0.02446	0.00655	0.00210	0.00079	0.00081	—
450	0.11585	0.04698	0.01763	0.00764	0.00404	0.00548	—
500	0.13365	0.06738	0.03289	0.01821	0.01317	0.02286	—
600	0.13013	0.07984	0.05156	0.03814	0.04072	0.09703	—
700	0.11346	0.07309	0.05221	0.04407	0.05900	0.17309	—
800	0.09936	0.06444	0.04732	0.04241	0.06448	0.22100	0.00001
900	0.08822	0.05710	0.04235	0.03873	0.06317	0.24218	0.00001
1,000	0.07929	0.05126	0.03798	0.03508	0.05871	0.24513	0.00001
1,250	0.06358	0.04104	0.03041	0.02820	0.04796	0.22260	0.00001
1,500	0.05286	0.03429	0.02530	0.02351	0.04016	0.19461	0.00002
1,750	0.04544	0.02937	0.02172	0.02016	0.03447	0.16986	0.00002
2,000	0.03967	0.02567	0.01898	0.01767	0.03015	0.14960	0.00002
	0°						
	S^{8+}	S^{9+}	S^{10+}	S^{11+}	S^{12+}	S^{13+}	S^{14+}
125	—	—	—	—	—	—	—
150	0.00003	—	—	—	—	—	—
175	0.00013	—	—	—	—	—	—
200	0.00059	0.00002	—	—	—	—	—
250	0.00446	0.00034	0.00003	—	—	—	—
300	0.01729	0.00228	0.00027	0.00004	0.00001	0.00001	—
350	0.04327	0.00885	0.00161	0.00039	0.00010	0.00008	—
400	0.07851	0.02398	0.00643	0.00208	0.00079	0.00080	—
450	0.10991	0.04587	0.01727	0.00754	0.00401	0.00545	—
500	0.12520	0.06542	0.03209	0.01792	0.01303	0.02270	—
600	0.11818	0.07634	0.04964	0.03722	0.04008	0.09601	—
700	0.09954	0.06848	0.04930	0.04246	0.05760	0.17038	—
800	0.08401	0.05901	0.04362	0.04015	0.06224	0.21602	0.00001
900	0.07178	0.05101	0.03800	0.03592	0.06010	0.23461	0.00001
1,000	0.06198	0.04462	0.03310	0.03181	0.05491	0.23493	0.00001
1,250	0.04481	0.03340	0.02456	0.02407	0.04274	0.20662	0.00001
1,500	0.03351	0.02604	0.01891	0.01884	0.03400	0.17416	0.00001
1,750	0.02591	0.02080	0.01500	0.01517	0.02770	0.14617	0.00002
2,000	0.02028	0.01690	0.01208	0.01245	0.02294	0.12343	0.00001

Note. No opacity effects and the viewing angle of 0° are displayed for Atmosphere 2. The efficiency shown here is that solely from direct excitation collisions for sulfur.

Table B10

The X-Ray Efficiency ($[cm^2 sec]^{-1} [keV/u]^{-1}$) of Outgoing Photons as a Function of Initial Ion Energy Including Opacity Effects

Atmosphere 2 (Well-mixed atmosphere)							
Energy	80°						
(keV/u)	S^{8+}	S^{9+}	S^{10+}	S^{11+}	S^{12+}	S^{13+}	S^{14+}
125	—	—	—	—	—	—	—
150	0.00003	—	—	—	—	—	—
175	0.00012	—	—	—	—	—	—
200	0.00055	0.00002	—	—	—	—	—
250	0.00409	0.00033	0.00003	—	—	—	—
300	0.01540	0.00215	0.00026	0.00004	0.00001	0.00001	—
350	0.03736	0.00823	0.00151	0.00037	0.00009	0.00008	—
400	0.06542	0.02194	0.00594	0.00197	0.00076	0.00078	—
450	0.08778	0.04118	0.01573	0.00708	0.00384	0.00529	—
500	0.09491	0.05733	0.02874	0.01666	0.01242	0.02197	—
600	0.07866	0.06250	0.04193	0.03330	0.03726	0.09138	—
700	0.05722	0.05122	0.03823	0.03585	0.05161	0.15840	—
800	0.04149	0.03987	0.03044	0.03138	0.05297	0.19449	0.00001
900	0.03047	0.03094	0.02359	0.02560	0.04793	0.20287	0.00001
1,000	0.02265	0.02424	0.01820	0.02051	0.04058	0.19366	0.00001
1,250	0.01161	0.01385	0.01001	0.01203	0.02560	0.14807	0.00001
1,500	0.00648	0.00838	0.00588	0.00736	0.01646	0.10687	0.00001
1,750	0.00398	0.00532	0.00366	0.00475	0.01092	0.07632	0.00001
2,000	0.00260	0.00351	0.00238	0.00317	0.00740	0.05453	0.00001
	90°						
	S^{8+}	S^{9+}	S^{10+}	S^{11+}	S^{12+}	S^{13+}	S^{14+}
125	—	—	—	—	—	—	—
150	0.00002	—	—	—	—	—	—
175	0.00010	—	—	—	—	—	—
200	0.00041	0.00002	—	—	—	—	—
250	0.00278	0.00026	0.00002	—	—	—	—
300	0.00938	0.00160	0.00020	0.00003	0.00001	—	—
350	0.02037	0.00575	0.00109	0.00029	0.00008	0.00007	—
400	0.03168	0.01429	0.00409	0.00150	0.00063	0.00068	—
450	0.03694	0.02459	0.01017	0.00518	0.00306	0.00452	—
500	0.03333	0.03053	0.01721	0.01155	0.00963	0.01838	—
600	0.01713	0.02370	0.01902	0.01879	0.02510	0.06918	—
700	0.00752	0.01209	0.01157	0.01476	0.02803	0.10348	—
800	0.00386	0.00581	0.00583	0.00853	0.02127	0.10372	0.00001
900	0.00240	0.00313	0.00308	0.00447	0.01331	0.08419	0.00001
1,000	0.00168	0.00199	0.00184	0.00243	0.00747	0.06045	0.00001
1,250	0.00096	0.00099	0.00086	0.00098	0.00226	0.02403	0.00001
1,500	0.00066	0.00064	0.00058	0.00060	0.00108	0.01076	0.00001
1,750	0.00051	0.00047	0.00042	0.00045	0.00068	0.00539	0.00001
2,000	0.00042	0.00037	0.00033	0.00037	0.00047	0.00302	0.00001

Note. Viewing angles of 80° and 90° are displayed for Atmosphere 2. The efficiency shown here is that solely from direct excitation collisions for sulfur.

Appendix C: Discussion on Data Usage

In the appendix we have provided as much of the derived data as possible (the oxygen collision data made violable by Schultz et al., 2019) with the goal that anyone can use it to estimate their own X-ray flux as long as they have access to an initial JEDI spectrum. Here we want to layout as clearly as possible how to take an ion flux and produce an X-ray power.

1. The first, and arguably most difficult, part is converting the JEDI energy spectrogram into a usable ion flux. To be done accurately, this requires knowing the width of each energy bin on JEDI at the time of measurement. We have included the energy bin widths in Table B1 that correspond to the data in Figure 4. It is likely the energies bins will be changed and resized, if they have not already.
2. Once the bin widths are known, one can convert the intensity from counts/steradian/cm^2/s/keV to counts/cm^2/sec by multiplying each flux intensity by 2π and the corresponding energy bin width. A second thing to consider is that the first three energy bins cannot distinguish between oxygen and sulfur ions. In this study we used an O:S ratio of 2:1 to separate the flux in the first three energy bins, motivated by the likely source of SO_2 from Io's volcanoes. A different ratio can be used, but those low energies will not affect X-ray production, anyway.
3. Once an intensity of counts/cm^2/s versus ion energy (in keV/u, not total energy) is obtained, one can multiply the intensity by the ion energy (keV/u) and the X-ray efficiency for each charge state of the ion species at a given ion energy in Appendix A or B. To account for all X-rays, charge exchange and direct

Table C1
Example of Calculating X-Ray Production Rates Associated With JEDI Oxygen Ion Flux Measurements

Oxygen Energy (keV)	JEDI flux[a] (c/str/cm^2/s/keV)	Energy bin width (keV)	Intensity (c/cm^2/s)	Energy (keV/u)
171	249.9	66	103,631	11
240	339.7	71	151,542	15
324	279.0	105	184,066	20
477	219.8	216	298,306	30
746	89.50	346	194,571	47
956	43.61	251	68,776	60
1,240	22.56	300	42,525	78
1,930	8.687	880	48,032	121
3,490	3.018	2,280	43,235	218
7,300	0.914	5,340	30,667	456
Energy (keV/u)	X-ray efficiency[b] ([cm^{2}sec]$^{-1}$[keV/u]$^{-1}$)	X-ray production (photons/cm^2/s)		
11	0.0000	0.000		
15	0.0000	0.000		
20	0.0000	0.000		
30	0.0000	0.000		
47	0.0000	0.000		
60	0.0000	0.000		
78	0.0000	0.000		
121	0.0003	1.74×10^3		
218	0.0246	2.32×10^5		
456	0.2951	4.13×10^6		
Total power flux (μW/m^2):		4.2		

[a] These are the same flux measurements as those shown in Figure 4. [b] X-ray efficiency values in Appendix A or B. These values are the sum of O^{6+} and O^{7+} from both charge exchange and direct excitation for an exit angle of 80° in Atmosphere 1.

excitation need to be considered, in which case the X-ray efficiencies can be summed together. This will result in the number of photons/cm^2/s produced by each ion charge state and species.

4. Summing the photon production rate for each charge state together will give the total X-ray production rate for a given JEDI pass.
5. Multiplying the photon production rate by the average photon energy, 1.6×10^{-19} J/eV, 10^6 μW/W, and 10^4 cm^2/m^2 will yield the power in μW/m^2. In general, the average photon energy is likely between 500 and 600 eV. If sulfur emission is higher than oxygen, then 500 eV is more accurate, and if oxygen emission is greater, the average photon energy probably tends closer to 600 eV.

As an example, for the JEDI oxygen measurement discussed in this text, the total photon production and power is calculated at each step in Table B1.

The total X-ray production shown in Table B1 is only about 7% higher than what is shown in Figure 12, where the power flux was found by integrating over every photon energy. This exact same process can be used for sulfur, but in this example sulfur emission is much less than oxygen.

Acknowledgments
This work was supported at the University of Kansas by NASA Grant NNX14AG79G. See supporting information for data used to produce the figures and tables in this paper. Data associated with the ion precipitation model used here can be found on the corresponding AGU website, and all X-ray data presented here are publicly available on the XMM-Newton Science archive (https://nxsa.esac.esa.int/nxsa-web/#search).

References

Branduardi-Raymont, G., Bhardwaj, A., Elsner, R. F., Gladstone, G. R., Ramsay, G., Rodriguez, P., et al. (2007). A study of Jupiter's aurorae with XMM-Newton. *Astronomy and Astrophysics*, *463*(2), 761–774. https://doi.org/10.1051/0004-6361:20066406

Branduardi-Raymont, G., Elsner, R. F., Galand, M., Grodent, D., Cravens, T. E., Ford, P., et al. (2008). Spectral morphology of the X-ray emission from Jupiter's aurorae. *Journal of Geophysical Research*, *113*, A02202. https://doi.org/10.1029/2007JA012600

Branduardi-Raymont, G., Elsner, R. F., Gladstone, G. R., Ramsay, G., Rodriguez, P., Soria, R., & Waite, J. H. (2004). First observation of Jupiter by XMM-Newton. *Astronomy and Astrophysics*, *424*(1), 331–337. https://doi.org/10.1051/0004-6361:20041149

Clark, G., Mauk, B. H., Haggerty, D., Paranicas, C., Kollmann, P., Rymer, A., et al. (2017). Energetic particle signatures of magnetic field-aligned potentials over Jupiter's polar regions. *Geophysical Research Letters*, *44*, 8703–8711. https://doi.org/10.1002/2017GL074366

Clark, G., Mauk, B. H., Paranicas, C., Haggerty, D., Kollmann, P., Rymer, A., et al. (2017). Observation and interpretation of energetic ion conics in Jupiter's polar magnetosphere. *Geophysical Research Letters*, *44*, 4419–4425. https://doi.org/10.1002/2016GL072325

Clark, G., Tao, C., Mauk, B. H., Nichols, J., Saur, J., Bunce, E. J., et al. (2018). Precipitating electron energy flux and characteristic energies in Jupiter's main auroral region as measured by Juno/JEDI. *Journal of Geophysical Research: Space Physics*, *123*, 7554–7567. https://doi.org/10.1029/2018JA025639

Connerney, J. E. P., Adriani, A., Allegrini, F., Bagenal, F., Bolton, S. J., Bonfond, B., et al. (2017). Jupiter's magnetosphere and aurorae observed by the Juno spacecraft during its first polar orbits. *Science*, *356*(6340), 826–832. https://doi.org/10.1126/science.aam5928

Connerney, J. E. P., Kotsiaros, S., Oliversen, R. J., Espley, J. R., Joergensen, J. L., Joergensen, P. S., et al. (2018). A new model of Jupiter's magnetic field from Juno's first nine orbits. *Geophysical Research Letters*, *45*, 2590–2596. https://doi.org/10.1002/2018GL077312

Cravens, T. E., Clark, J., Bhardwaj, A., Elsner, R., Waite Jr., J. H., Maurellis, A. N., et al. (2006). X-ray emission from the outer planets: Albedo for scattering and fluorescence of solar X rays. *Journal of Geophysical Research: Space Physics*, *111*, A07308. https://doi.org/10.1029/2005JA011413

Cravens, T. E., Howell, E., Waite, J. H., & Gladstone, G. R. (1995). Auroral oxygen precipitation at Jupiter. *Journal of Geophysical Research*, *100*(A9), 17,153–17,161. https://doi.org/10.1029/95JA00970

Cravens, T. E., Waite, J. H., Gombosi, T. I., Lugaz, N., Gladstone, G. R., Mauk, B. H., & MacDowall, R. J. (2003). Implications of Jovian X-ray emission for magnetosphere-ionosphere coupling. *Journal of Geophysical Research*, *108*(A12), 1465. https://doi.org/10.1029/2003JA010050

Delamere, P. A., Bagenal, F., & Steffl, A. (2005). Radial variations in the Io plasma torus during the Cassini era. *Journal of Geophysical Research*, *110*, A12223. https://doi.org/10.1029/2005JA011251

Dougherty, L. P., Bodisch, K. M., & Bagenal, F. (2017). Survey of Voyager plasma science ions at Jupiter: 2. Heavy ions. *Journal of Geophysical Research: Space Physics*, *122*, 8257–8276. https://doi.org/10.1002/2017JA024053

Dunn, W. R., Branduardi-Raymont, G., Elsner, R. F., Vogt, M. F., Lamy, L., Ford, P. G., et al. (2016). The impact of an ICME on the Jovian X-ray aurora. *Journal of Geophysical Research: Space Physics*, *121*, 2274–2307. https://doi.org/10.1002/2015JA021888

Dunn, W. R., Branduardi-Raymont, G., Ray, L. C., Jackman, C. M., Kraft, R. P., Elsner, R. F., et al. (2017). The independent pulsations of Jupiter's northern and southern X-ray auroras. *Nature Astronomy*, *1*(11), 758–764. https://doi.org/10.1038/s41550-017-0262-6

Elsner, R. F., Lugaz, N., Waite, J. H., Cravens, T. E., Gladstone, G. R., Ford, P., et al. (2005). Simultaneous Chandra X-ray, Hubble Space Telescope ultraviolet, and Ulysses radio observations of Jupiter's aurora. *Journal of Geophysical Research*, *110*, A01207. https://doi.org/10.1029/2004JA010717

Folkner, W. M., Iess, L., Anderson, J. D., Asmar, S. W., Buccino, D. R., Durante, D., et al. (2017). Jupiter gravity field estimated from the first two Juno orbits. *Geophysical Research Letters*, *44*, 4694–4700. https://doi.org/10.1002/2017GL073140

Gérard, J.-C., Bonfond, B., Grodent, D., Radioti, A., Clarke, J. T., Gladstone, G. R., et al. (2014). Mapping the electron energy in Jupiter's aurora: Hubble spectral observations. *Journal of Geophysical Research: Space Physics*, *119*, 9072–9088. https://doi.org/10.1002/2014JA020514

Gladstone, G. R., Waite, J. H., Grodent, D., Lewis, W. S., Crary, F. J., Elsner, R. F., et al. (2002). A pulsating auroral X-ray hot spot on Jupiter. *Nature*, *415*(6875), 1000–1003. https://doi.org/10.1038/4151000a

Grozdanov, T. P., & Janev, R. K. (1978). One-electron capture in slow collisions of highly charged ions with atoms. *Physics Letters A*, *66*(3), 191–194. https://doi.org/10.1016/0375-9601(78)90653-9

Haggerty, D. K., Mauk, B. H., Paranicas, C. P., Clark, G., Kollmann, P., Rymer, A. M., et al. (2017). Juno/JEDI observations of 0.01 to >10 MeV energetic ions in the Jovian auroral regions: Anticipating a source for polar X-ray emission. *Geophysical Research Letters*, *44*, 6476–6482. https://doi.org/10.1002/2017GL072866

Houston, S. J., Ozak, N., Young, J., Cravens, T. E., & Schultz, D. R. (2018). Jovian auroral ion precipitation: Field-aligned currents and ultraviolet emissions. *Journal of Geophysical Research: Space Physics*, *123*, 2257–2273. https://doi.org/10.1002/2017JA024872

Hui, Y., Schultz, D. R., Kharchenko, V. A., Bhardwaj, A., Branduardi-Raymont, G., Stancil, P. C., et al. (2010). Comparative analysis and variability of the Jovian X-ray spectra detected by the Chandra and XMM-Newton observatories. *Journal of Geophysical Research*, *115*, A07102. https://doi.org/10.1029/2009JA014854

Iess, L., Folkner, W. M., Durante, D., Parisi, M., Kaspi, Y., Galanti, E., et al. (2018). Measurement of Jupiter's asymmetric gravity field. *Nature*, *555*, 220–222. https://doi.org/10.1038/nature25776

Jackman, C. M., Knigge, C., Altamirano, D., Gladstone, R., Dunn, W., Elsner, R., et al. (2018). Assessing quasi-periodicities in Jovian X-ray emissions: Techniques and heritage survey. *Journal of Geophysical Research: Space Physics*, *123*, 9204–9221. https://doi.org/10.1029/2018JA025490

Kim, T. K., Ebert, R. W., Valek, P. W., Allegrini, F., McComas, D. J., Bagenal, F., et al. (2019). Method to derive ion properties from Juno JADE including abundance estimates for O^+ and S^{2+}. *Journal of Geophysical Research: Space Physics*, *124*. https://doi.org/10.1029/2018JA026169

Mauk, B. H., Haggerty, D. K., Jaskulek, S. E., Schlemm, C. E., Brown, L. E., Cooper, S. A., et al. (2017). The Jupiter Energetic Particle Detector Instrument (JEDI) investigation for the Juno mission. *Space Science Reviews*, *213*(1), 289–346. https://doi.org/10.1007/s11214-013-0025-3

Maurellis, A. N., & Cravens, T. E. (2001). Ionospheric effects of comet Shoemaker-Levy 9 impacts with Jupiter. *Icarus*, *154*(2), 350–371. https://doi.org/10.1006/icar.2001.6709

Metzger, A. E., Luthey, J. L., Gilman, D. A., Hurley, K. C., Schnopper, H. W., Seward, F. D., & Sullivan, J. D. (1983). The detection of X rays from Jupiter. *Journal of Geophysical Research*, *88*, 7731–7741. https://doi.org/10.1029/JA088iA10p07731

Moore, K. M., Yadav, R. K., Kulowski, L., Cao, H., Bloxham, J., Connerney, J. E. P., et al. (2018). A complex dynamo inferred from the hemispheric dichotomy of Jupiter's magnetic field. *Nature*, *561*(7721), 76–78. https://doi.org/10.1038/s41586-018-0468-5

Olson, R. E. (1981). n, l distributions in $A^{q+} + \mathrm{H}$ electron-capture collisions. *Physical Review A*, *24*, 1726–1733. https://doi.org/10.1103/PhysRevA.24.1726

Oppenheimer, J. R. (1928). On the quantum theory of the capture of electrons. *Physical Review*, *31*, 349–356. https://doi.org/10.1103/PhysRev.31.349

Orton, G. S., Hansen, C., Caplinger, M., Ravine, M., Atreya, S., Ingersoll, A. P., et al. (2017). The first close-up images of Jupiter's polar regions: Results from the Juno mission JunoCam instrument. *Geophysical Research Letters*, *44*, 4599–4606. https://doi.org/10.1002/2016GL072443

Ozak, N., Cravens, T. E., & Schultz, D. R. (2013). Auroral ion precipitation at Jupiter: Predictions for Juno. *Geophysical Research Letters*, *40*, 4144–4148. https://doi.org/10.1002/grl.50812

Ozak, N., Schultz, D. R., Cravens, T. E., Kharchenko, V., & Hui, Y.-W. (2010). Auroral X-ray emission at Jupiter: Depth effects. *Journal of Geophysical Research*, *115*, A11306. https://doi.org/10.1029/2010JA015635

Parkinson, C. D., Stewart, A. I. F., Wong, A. S., Yung, Y. L., & Ajello, J. M. (2006). Enhanced transport in the polar mesosphere of Jupiter: Evidence from Cassini UVIS helium 584 Åairglow. *Journal of Geophysical Research*, *111*, E02002. https://doi.org/10.1029/2005JE002539

Radioti, A., Krupp, N., Woch, J., Lagg, A., Glassmeier, K.-H., & Waldrop, L. S. (2005). Ion abundance ratios in the Jovian magnetosphere. *Journal of Geophysical Research*, *110*, A07225. https://doi.org/10.1029/2004JA010775

Radioti, A., Krupp, N., Woch, J., Lagg, A., Glassmeier, K.-H., & Waldrop, L. S. (2006). Correction to "Ion abundance ratios in the Jovian magnetosphere". *Journal of Geophysical Research*, *111*, A10224. https://doi.org/10.1029/2006JA011990

Sada, P. V., Bjoraker, G. L., Jennings, D. E., McCabe, G. H., & Romani, P. N. (1998). Observations of CH_4, C_2H_6, and C_2H_2 in the stratosphere of Jupiter. *Icarus*, *136*(2), 192–201. https://doi.org/10.1006/icar.1998.6021

Sánchez-Lavega, A., Hueso, R., Eichstädt, G., Orton, G., Rogers, J., Hansen, C. J., et al. (2018). The rich dynamics of Jupiter's Great Red Spot from JunoCam: Juno images. *Astronomical Journal*, *156*, 162. https://doi.org/10.3847/1538-3881/aada81

Schultz, D. R., Gharibnejad, H., Cravens, T. E., & Houston, S. J. (2019). Data for secondary-electron production from ion precipitation at Jupiter II: Simultaneous and non-simultaneous target and projectile processes in collisions of $O^{q+} + H_2$ ($q = 0$–8). *Atomic Data and Nuclear Data Tables*, *126*, 1–69. https://doi.org/10.1016/j.adt.2018.08.002

Schultz, D. R., Lee, T.-G., & Loch, S. D. (2010). Calculations and analysis of cross sections required for argon charge exchange recombination spectroscopy. *Journal of Physics B: Atomic, Molecular and Optical Physics*, *43*(14), 144002. https://doi.org/10.1088/0953-4075/43/14/144002

Schultz, D. R., Ozak, N., Cravens, T. E., & Gharibnejad, H. (2017). Ionization of molecular hydrogen and stripping of oxygen atoms and ions in collisions of $O^{q+} + H_2$ ($q = 0$–8): Data for secondary electron production from ion precipitation at Jupiter. *Atomic Data and Nuclear Data Tables*, *113*, 1–116. https://doi.org/10.1016/j.adt.2016.04.003

Seiff, A., Kirk, D. B., Knight, T. C. D., Mihalov, J. D., Blanchard, R. C., Young, R. E., et al. (1996). Structure of the atmosphere of Jupiter: Galileo probe measurements. *Science*, *272*(5263), 844–845. https://doi.org/10.1126/science.272.5263.844

Seiff, A., Kirk, D. B., Knight, T. C. D., Young, L. A., Milos, F. S., Venkatapathy, E., et al. (1997). Thermal structure of Jupiter's upper atmosphere derived from the Galileo probe. *Science*, *276*(5309), 102–104. https://doi.org/10.1126/science.276.5309.102

Sinclair, J. A., Orton, G. S., Greathouse, T. K., Fletcher, L. N., Moses, J. I., Hue, V., & Irwin, P. G. J. (2018). Jupiter's auroral-related stratospheric heating and chemistry II: Analysis of IRTF-TEXES spectra measured in December 2014. *Icarus*, *300*, 305–326. https://doi.org/10.1016/j.icarus.2017.09.016